This is the accepted manuscript of an article that has been accepted for publication in InterPore Journal. The final version of record will appear in a future issue and may differ slightly from this version.

InterPore JOURNAL

ACCEPTED ARTICLE

PETROPHYSICAL CHARACTERIZATION OF INDIANA LIMESTONE USING MEDICAL DUAL-ENERGY COMPUTED TOMOGRAPHY TECHNIQUE: INSIGHTS INTO POROSITY, BULK DENSITY, AND EFFECTIVE ATOMIC NUMBER

Walter L. F. Antelo[1], Janeth A. Vidal Vargas[2], Rosangela B. Z. L. Moreno[3]

[1 2 3]*Laboratory for Oil Reservoir (LABORE), Faculty of Mechanical Engineering (FEM), Universidade Estadual de Campinas (UNICAMP), Cidade Universitária, Barão Geraldo, SP*

Correspondence to:
Walter L. F. Antelo, walterleo.antelo@gmail.com

How to Cite:
Flores Antelo, W. L. (2026 accepted article). Petrophysical Characterization of Indiana Limestone Using Medical Dual-Energy Computed Tomography Technique: Insights into Porosity, Bulk Density, and Effective Atomic Number. *InterPore Journal*. https://doi.org/10.69631/s3tb8r43

RECEIVED: 16 Jun. 2025
ACCEPTED: 16 Nov. 2025
PUBLISHED Online: 10 Mar. 2026

ABSTRACT

Computed Tomography (CT) enables non-destructive 3D reconstruction of pore structures and rock properties mapping. Typically, such images are obtained from micro-CT (µm-scale) or synchrotron imaging (nm-scale). Despite their accuracy, these high-resolution imaging methods are expensive, time-consuming, and limited in sample size, affecting representative volume analysis. This work investigates an alternative approach using medical-CT (100 µm resolution), applying the dual-energy CT technique (DECT) to characterize petrophysical properties (total porosity, bulk density, and effective atomic number) of six Indiana limestone samples (3.81 cm diameter, 4.88 cm length). Samples with porosities between 17.5% and 19.1% were scanned using paired high-energy (130 kV) and low-energy (80 kV) protocols, allowing DECT analysis to generate detailed 2D and 3D property maps. Additionally, the single-energy CT (SECT) technique, enhanced by subtracting images of the rock sample in saturated and dry conditions, improved the estimation of effective porosity. DECT and SECT results, processed with Python scripts and Avizo 3D, demonstrated average differences of 3.34% for bulk density, 5.30% for effective porosity, and 4.65% for effective atomic number compared to basic petrophysics measurements. Although artifacts from low-energy scans presented limitations, their impact can be reduced by optimizing acquisition parameters, improving the experimental setup, and applying reconstruction filtering techniques. Overall, this study highlights medical-CT as a fast, cost-effective method for analyzing larger samples, providing a practical alternative to tra-

ditional high-resolution imaging to estimate key petrophysical properties for the identification and visualization of heterogeneity on carbonates rocks.

KEYWORDS
Digital Rock Physics, Petrophysics, DECT, Medical-CT

© 2026 The Authors

This is an open access article published by InterPore under the terms of the Creative Commons Attribution-NonCommercial-NoDerivatives 4.0 International License (CC BY-NC-ND 4.0) (https://creativecommons.org/licenses/by-nc-nd/4.0/).

1. INTRODUCTION

The evolution of computed tomography (CT), from its invention by Hounsfield in 1972 to recent advances, has significantly impacted petrophysical studies in reservoir rocks. Early work, such as the determination of porosity and density from digital images [45], paved the way for innovations, such as dual-energy CT (DECT) [2, 35, 34], which uses high- and low-energy scans to more accurately determine petrophysical properties. These advancements have led to detailed studies on fluid flow visualization through porous media [1], and multiphase flow simulations based on Navier-Stokes and Lattice-Boltzmann transport equations [30, 31].

With advancements in tomography technologies, imaging at smaller resolution scales is now possible: down to the millimeter scale (10^{-3} m) with medical-CT, the micrometer scale (10^{-6} m) with industrial-CT, and the nanometer scale (10^{-9} m) with Synchrotron-Beamline [23, 47]. However, as resolution increases, the sample size decreases, which is an important aspect when considering upscaling to field scales (10^{3} m). For this reason, millimeter-scale imaging becomes relevant as it allows the analysis of relatively large samples, typically up to 30 cm in length, with a maximum of 100 cm in some cases. Originally developed for medical diagnostics, DECT was initially used to distinguish regions with similar CT numbers (CTN) that could not be differentiated using conventional single-energy imaging. Extending these capabilities, DECT has been adapted to geosciences for more accurate rock property characterization by calibration processes.

Dual-energy computed tomography (DECT) can be applied at different imaging scales, including medical-CT [2], micro-CT [41], and synchrotron-CT [19, 36]. However, as reported in the literature [14], despite the superior resolution and image quality offered by industrial-CT systems, their high acquisition time and operational costs often pose significant limitations when compared to medical CT scanners. Basic industrial CT setups, equipped with 225 kV micro-focus capabilities, typically range in cost from €300,000 to over €1,000,000. In contrast, medical CT systems are generally more accessible, with prices ranging from €60,000 to €300,000, depending on the model and specifications. Furthermore, scan time greatly impacts the cost-effectiveness of each modality. Industrial-CT systems often require 30 to 60 minutes per scan, depending on the desired image quality [29], whereas medical-CT scanners can complete a full scan in approximately 5 seconds, plus a short cool-down period. This time efficiency allows medical CT scanners to image up to 10 samples within the time it takes to complete a single scan using an industrial-CT system, making them a more practical and cost-effective solution for routine laboratory workflows.

In carbonate rocks characterization, which are well known for their complex pore size distribution (PSD), as well presented in Figure1b that shows a mercury injection capillary pressure (MICP) curves extracted from the literature [27], which clearly illustrate the wide heterogeneity in pore radius, ranging from nano- to micro- and macro-pores (including vuggy porosity). The presence of these macro-pores makes medical-CT (also referred to as hospital-CT) a valuable imaging technique for identifying and visualizing such macroscopic features (≥100 □m). As shown in Figure1a [11], medical-CT imaging effectively complements the pore size range that cannot be fully captured by micro-CT (μm), thus enhancing multiscale pore structure characterization.

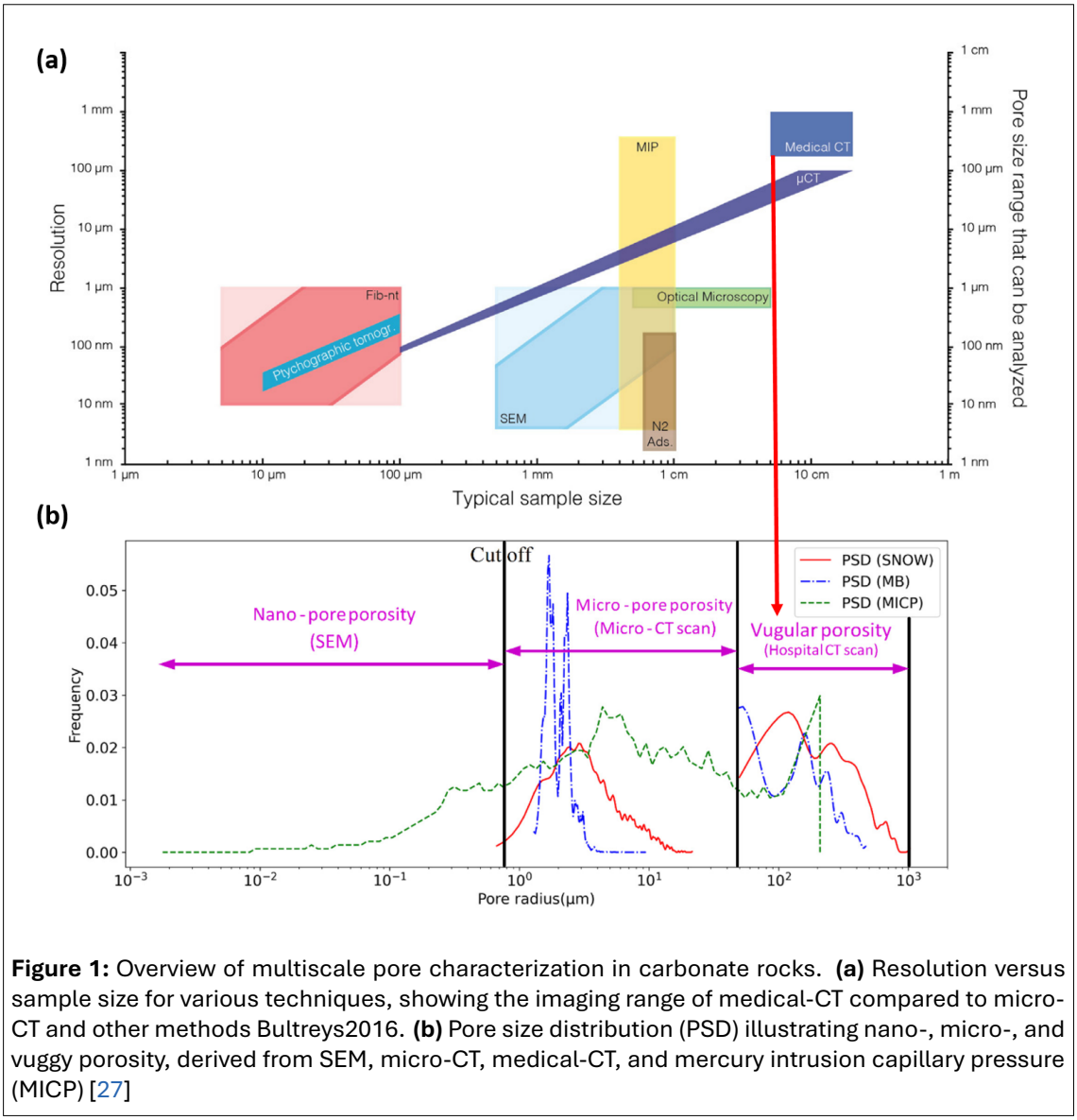

Figure 1: Overview of multiscale pore characterization in carbonate rocks. **(a)** Resolution versus sample size for various techniques, showing the imaging range of medical-CT compared to micro-CT and other methods Bultreys2016. **(b)** Pore size distribution (PSD) illustrating nano-, micro-, and vuggy porosity, derived from SEM, micro-CT, medical-CT, and mercury intrusion capillary pressure (MICP) [27]

This work aims to characterize key petrophysical properties, including total and effective porosity, bulk density, and effective atomic number, of six Indiana limestone samples using medical-CT digital imaging. Single- and dual-energy CT techniques (SECT [20] and DECT [2]) are applied to obtain these properties, which are then compared with basic petrophysics measurements to assess the accuracy of the methodology. The results are presented as 2D and 3D maps, profiles, and average values, allowing for both the quantification and visualization of the heterogeneity in these carbonate rocks.

2. MATERIALS AND METHODS

2.1. Rock sample description

Six rock samples, representing outcrops of Indiana limestone carbonate, were selected for petrophysical characterization using medical-CT imaging techniques. Each sample has a diameter of 3.81 cm and a length of around 5 cm. Basic petrophysics measurements were conducted to describe the samples used in this study, with the results presented in Table 1. The bulk density of the samples ranges from 2.13 to 2.17 g/cm

Basic petrophysical measurements were conducted to characterize the samples used in this study, and the results are presented in Table 1. The bulk density of the samples ranges from 2.13 to 2.17 g/cm^3. These relatively low values are attributed to the higher percentage of void space, as noted by [38]. The

Table 1: Basic petrophysical properties of Indiana limestone samples, including dimensions (measured with a caliper), bulk density (from mass and volume), and porosity and permeability (measured using gas porosimeter and permeability meter).

Sample Number	Sample ID	Diameter D (cm)	Length L (cm)	Bulk Density ρ_b (g/cm^3)	Porosity ϕ_{eff} (%)	Permeability k (mD)
1	ILH2A-1	3.820 ± 0.001	4.950 ± 0.002	2.143 ± 0.001	18.27 ± 0.37	36.53 ± 0.32
2	ILH2A-2	3.805 ± 0.001	4.710 ± 0.002	2.167 ± 0.001	17.48 ± 0.37	28.40 ± 0.25
3	ILH2A-3	3.810 ± 0.001	4.808 ± 0.002	2.150 ± 0.001	17.73 ± 0.37	27.72 ± 0.24
4	ILH2A-4	3.809 ± 0.001	4.919 ± 0.002	2.152 ± 0.001	17.60 ± 0.37	27.37 ± 0.24
5	ILH2A-5	3.805 ± 0.001	4.826 ± 0.002	2.143 ± 0.001	17.97 ± 0.36	35.20 ± 0.31
6	ILH2A-6	3.805 ± 0.001	4.995 ± 0.002	2.125 ± 0.001	19.13 ± 0.38	34.69 ± 0.30
Average		3.809	4.880	2.147	18.03	31.65

gas porosimeter measurements show the highest porosity value of 19.1% for sample 6 (ILH2A-6) and the lowest value of 17.5% for sample 2 (ILH2A-2). Although the porosity exhibits relatively high values, the average permeability of the samples is 31.7 mD. This discrepancy suggests that permeability does not scale proportionally with porosity, which may indicate a high degree of heterogeneity in the rock. Such heterogeneity is a well-known characteristic of Indiana limestone, which features a complex pore structure, including significant microporosity. This network of small pores can restrict fluid flow, leading to lower permeability despite high porosity values.

2.2. Rock sample medical-CT scan

In the medical-CT scanning process, the Beer-Lambert law (Eq.(1)) describes the predominant physical phenomenon. As shown in Figure2a, an X-ray source rotates around the rock sample, emitting X-rays beams with a given incident intensity I_o. These X-rays beams penetrate a thin thickness of the rock sample, effectively dividing it into a stack of slices, where the thickness of each slice depends directly on the resolution of the equipment. After passing through the sample, the remaining X-rays intensity I is recorded by detectors positioned parallel to both, the sample and the X-ray source. The linear attenuation coefficient mu is then obtained from the ratio I/I_o. Next, all the projections are reconstructed using a mathematical algorithm based on the Fourier transform (filtered back projection) to create cross-sectional images (slices) of attenuation coefficients $mu(h,x)$. Finally, the attenuation data from the tomographic process are normalized Eq.(2) and defined as CT number (CTN), which are commonly expressed on an internationally standardized scale known as Hounsfield Units (HU). On this scale, air is defined as -1000 HU and water as 0 HU. Each Hounsfield Unit (HU) corresponds to a 0.1% variation in density relative to the calibration reference scale [45, 46, 4].

$$\ln\left(\frac{I}{I_0}\right) = \int_0^L \mu(h(x,y))\, dh \tag{1}$$

$$\text{CTN} = \left(\frac{\mu - \mu_{\text{water}}}{\mu_{\text{water}}}\right) \times 1000 \tag{2}$$

Figure 2b shows the experimental setup used in this work to obtain the tomographic images of the studied samples. The setup consists of a Siemens SOMATOM® Emotion medical-CT scanner, capable of acquiring 16 images per second with a voxel resolution of 100x100x700 micrometers. The rock sample is placed into a glass holder with an atmospheric pressure (14.7 psi) and room temperature of 20 °C. Scanning is performed under two conditions (dry and saturated) for SECT application and two energy levels (130 kV and 80 kV) for DECT application. A detailed CT acquisition and reconstruction protocol is presented in the Table 2.

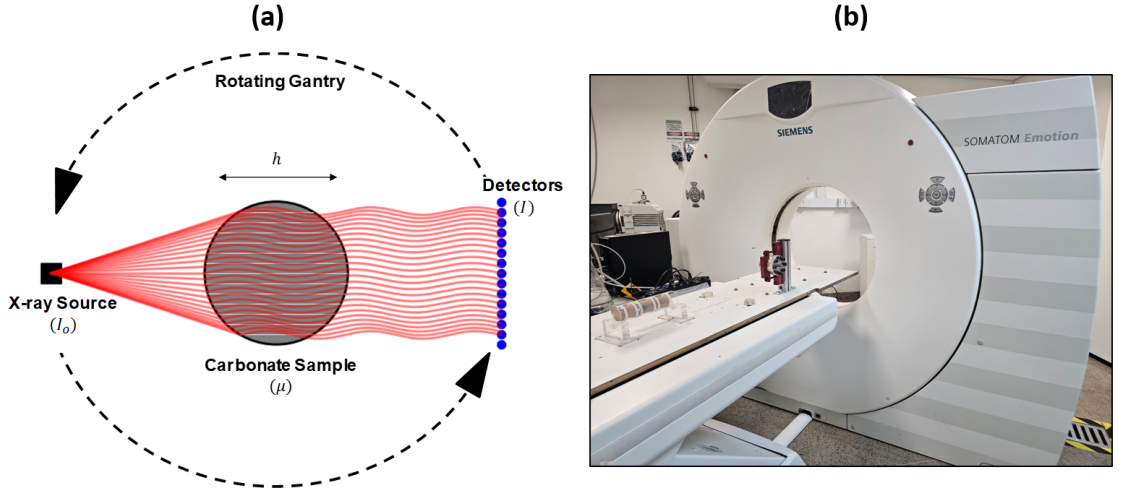

Figure 2: Medical-CT Scanner: (a) Imaging principles (adapted from [47]) and (b) experimental setup used in this work.

Table 2: Acquisition and reconstruction parameters used for high- and low-energy medical CT scans. Includes voltage, current, exposure settings, and reconstruction configuration applied to image the rock samples.

Acquisition Parameter	High Energy Value	Low Energy Value	Unit
Voltage	130	80	kV
X-ray Tube Current	56	183	mA
Exposure Time	1.5		s
Spiral Pitch Factor	0.55		dimensionless
Effective mAs	150	500	mAs
Slice Thickness	0.75		mm
Body Part Examined	Head		
Reconstruction Parameter	**High Energy Value**	**Low Energy Value**	**Unit**
Field of view (FOV)	50		mm
Recon Increment	0.70		mm
Convolution Kernel	H30s		

2.3. CT images pre-processing

CT images are digitally represented as three-dimensional grids composed of volume elements known as voxels. Each voxel is assigned a numerical value, known as the CT number (CTN), which is expressed in Hounsfield Units (HU). These CT numbers are displayed using a grayscale colormap, where lower HU values (such as air at approximately -1000 HU) appear darker, and higher HU values (denser materials, such as bone or minerals) appear brighter. This grayscale representation allows for clear differentiation between distinct phases or components within the scanned object. Figure 3 provides an illustration of these concepts.

CT Image preprocessing was performed using Avizo 3D software [42], prior to the application of DECT and SECT, and included cropping, masking, and filtering steps. During cropping, the initial (inlet) and final (outlet) slices of the rock sample were removed due to artifacts that introduced shadows non-representative of the actual rock sample (see Figure 4a and b). Next, a masking procedure was applied to all slices excluding the external components, such as the glass holder and centralizers (see Figure 4c).

Finally, to improve image quality by reducing the inherent noise, a non-local means filter [10] was applied to the sample images, achieving a good smoothing result while preserving edges (see Figure 5). The non-

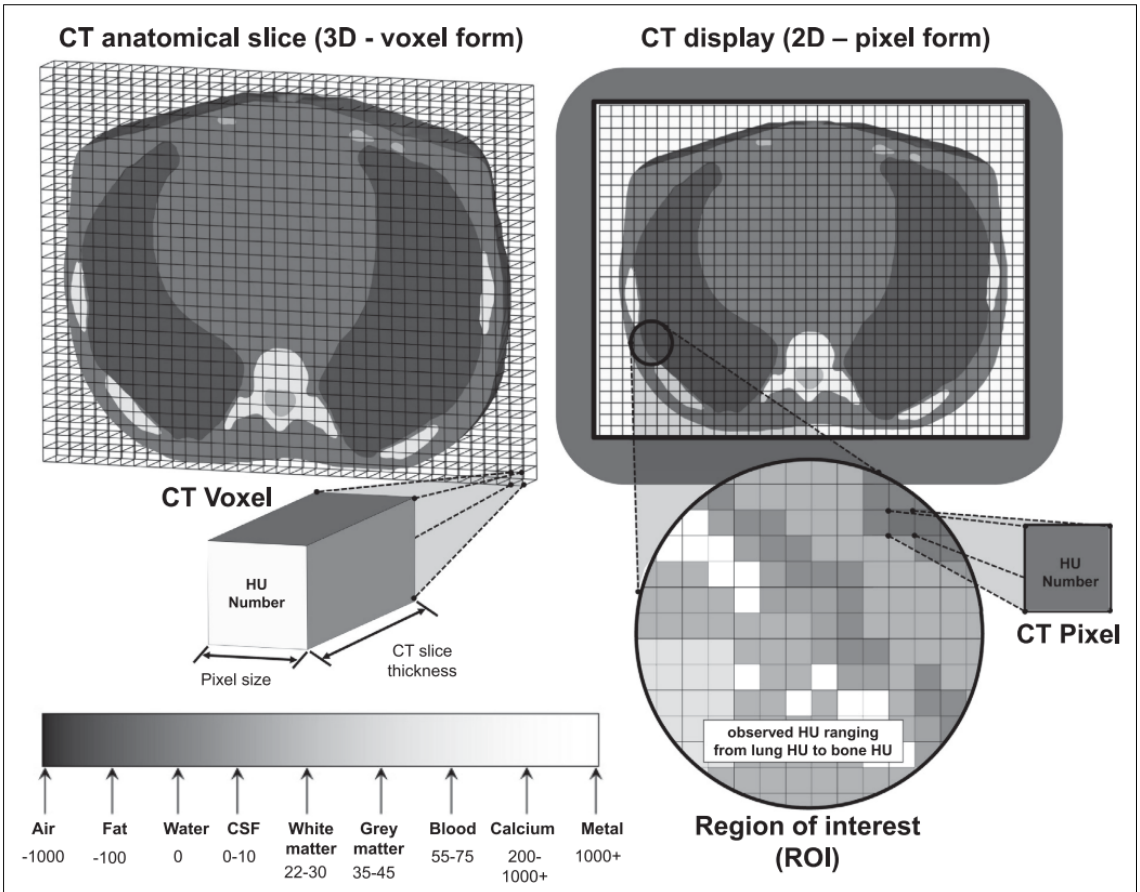

Figure 3: Schematic representation of a CT anatomical slice (left) and the corresponding CT image display (right) showing pixels (2D) and voxels (3D) in CT imaging. The HU spectrum is also illustrated, consisting of HU ranging from air (−1000 HU) to non-biological densities (metals, 1000+HU) [43].

local means filter was configured with the following parameters: noise standard deviation set to three times the automatically estimated value, patch size of 3 voxels, and search area of 6 voxels [39].

2.4. Dual-energy CT technique (DECT)

Unlike segmentation methods, which rely directly on image resolution, the DECT technique does not depend on visualizing pore structures to estimate porosity. In segmentation approaches, the image is binarized by labeling each voxel as either pore (1) or matrix (0), and porosity is calculated from the volume fraction of these labeled voxels. In contrast, the dual-energy technique estimates the bulk density of the entire sample using X-ray attenuation data (CTN). Microporosity, although visually unresolved by medical-CT due to resolution limits of 100 µm, still contributes to the attenuation signal (i.e., CT number), resulting in gray intensity tones in the image. These grayscale variations are processed by the DECT workflow, enabling the estimation of bulk density and, consequently, porosity, including the contribution from unresolved micropores as a fractal effect as shown in the Figure 6. In this way, DECT captures microporosity effects indirectly, treating them as part of the x-ray attenuation response, rather than requiring explicit visual identification. It is important to emphasize that DECT generates maps of porosity, bulk density, and effective atomic number, showing their spatial distribution along the rock sample. This allows the identification of regions with varying porosity values, without explicitly classifying each voxel as pore or matrix.

In the context of heterogeneous carbonate rocks (which are primarily composed of calcium-based minerals), DECT provides detailed insights into their complex structures and petrophysical properties. This approach can be combined with laboratory measurements and high-resolution subsampling to accu-

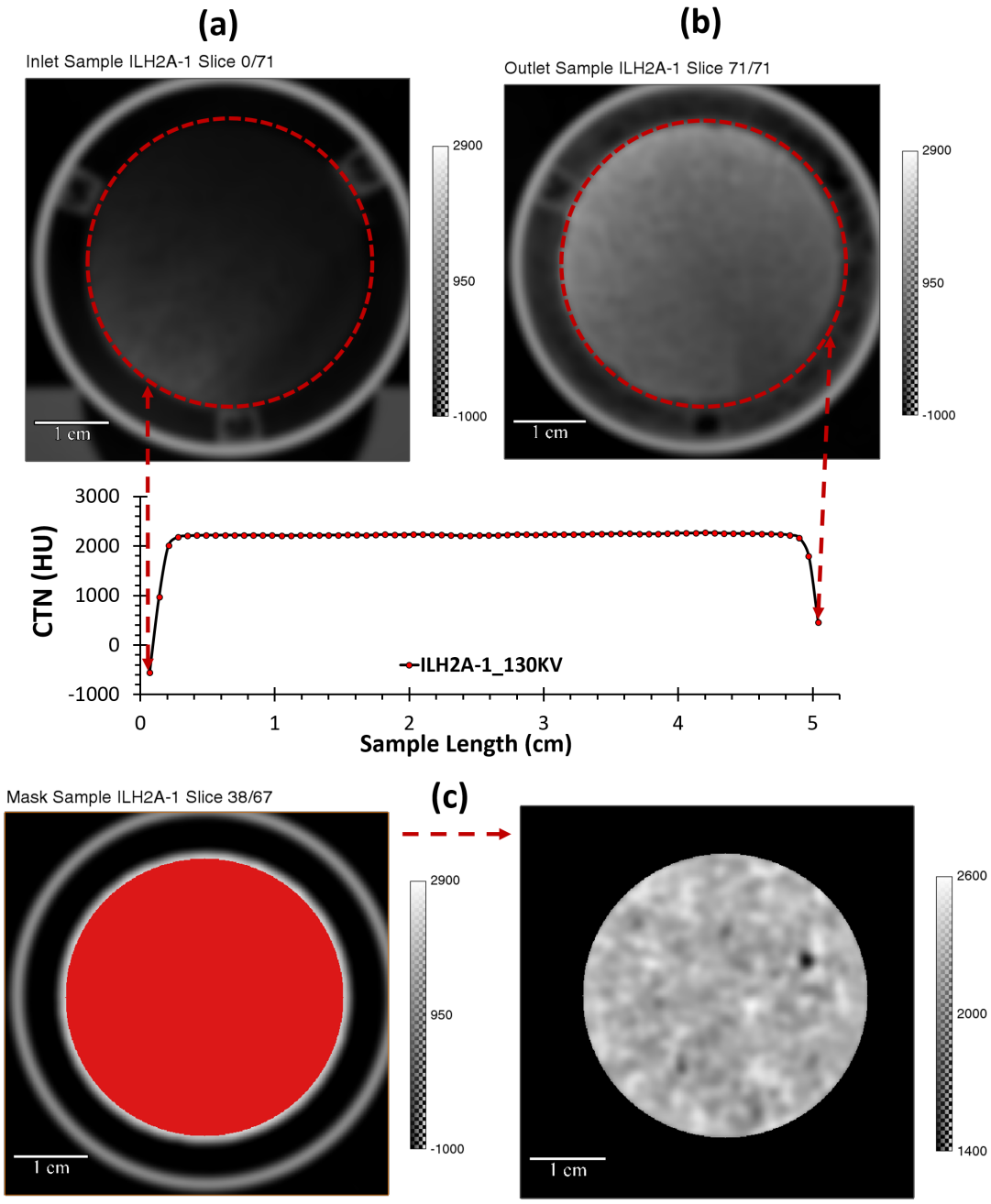

Figure 4: image preprocessing steps, showing cropping of CT slices at: (a) the inlet and (b) the outlet of the rock sample, followed by (c) mask application to isolate the region of interest.

rately estimate the total porosity of rock samples, including both connected and isolated pores, along with other parameters [40, 28, 32, 12, 24, 2]. This work applied DECT following the workflow shown in Figure 7, and 8.

The process begins with the acquisition of CT images of the rock sample along with three standard materials with known bulk densities (ρ_b) and effective atomic numbers (Z_{eff}). Each material, including the sample rock, was scanned twice using high-energy (130 kV) and low-energy (80 kV) protocols (Table 2).

During the processing stage, the average CT number (CTN) for three standard materials was calculated from both high- and low-energy scans. These values, along with the known bulk densities were used to formulate a system of three equations based on Eq.(3). This system can be solved using Cramer's

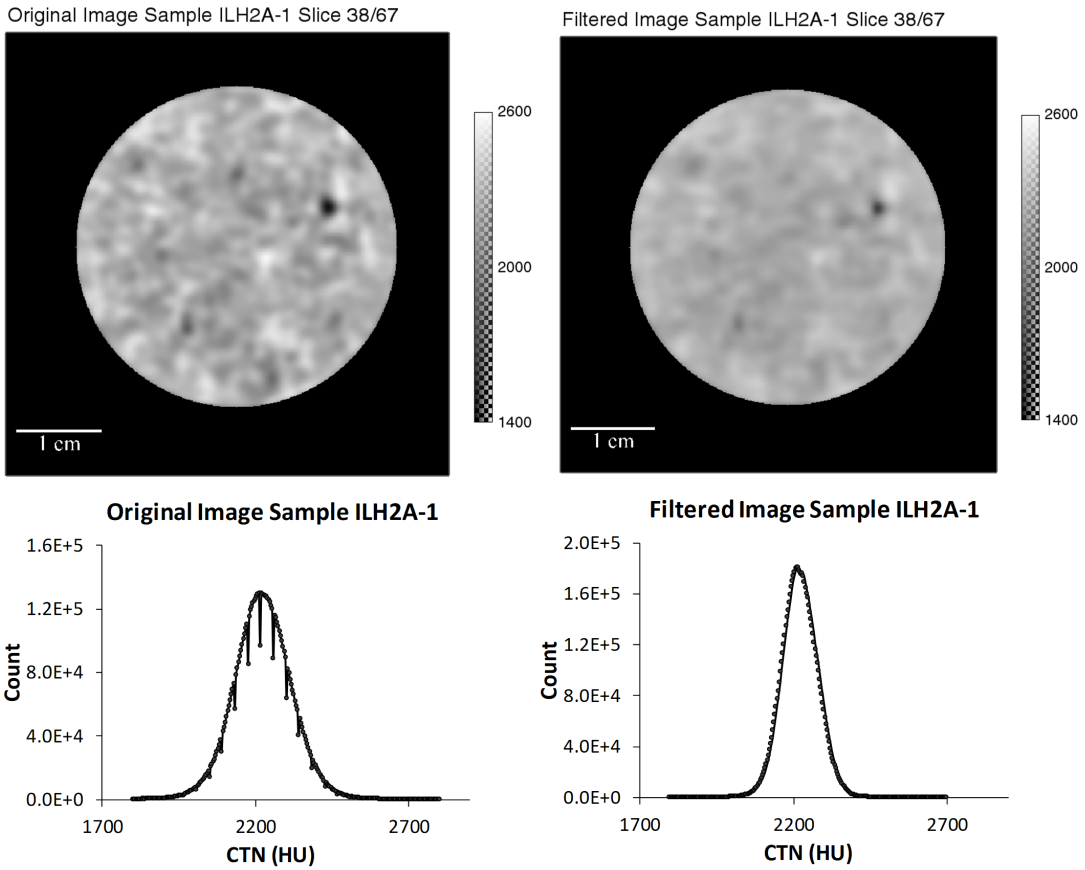

Figure 5: Comparison of original and filtered CT images (top) and their CT number histograms (bottom) for sample ILH2A-1, highlighting noise reduction and improved distribution sharpness after non-local means filtering.

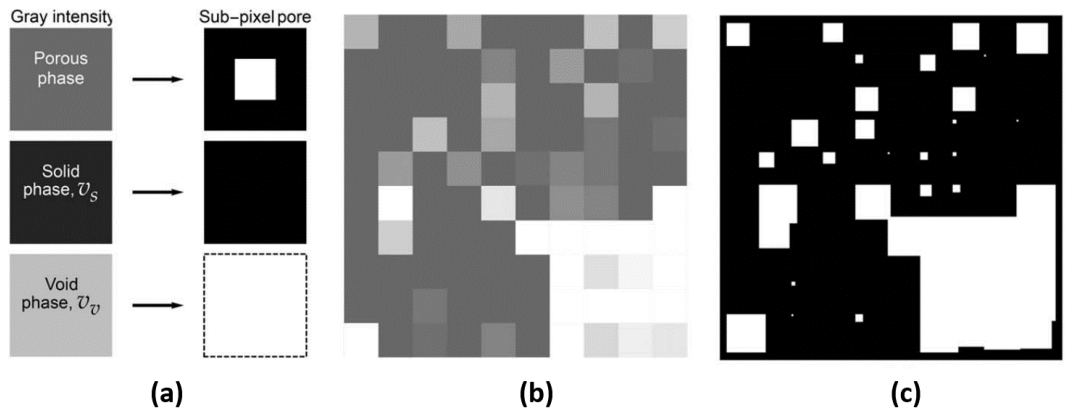

Figure 6: (a) Schematic showing the fractal effect from (left) grayscale pixel porosity (medical-CT) to a (right) sub-pixel resolution (micro-CT) with a binary structure of solid (black) and void (white) phases. (b, c) Example of downscaling from (b) a pixel porosity distribution to (c) a binary (black and white) image, where the average of these sub-pixel values is overlapping and represented as a grayscale pixel at the superior scale [21].

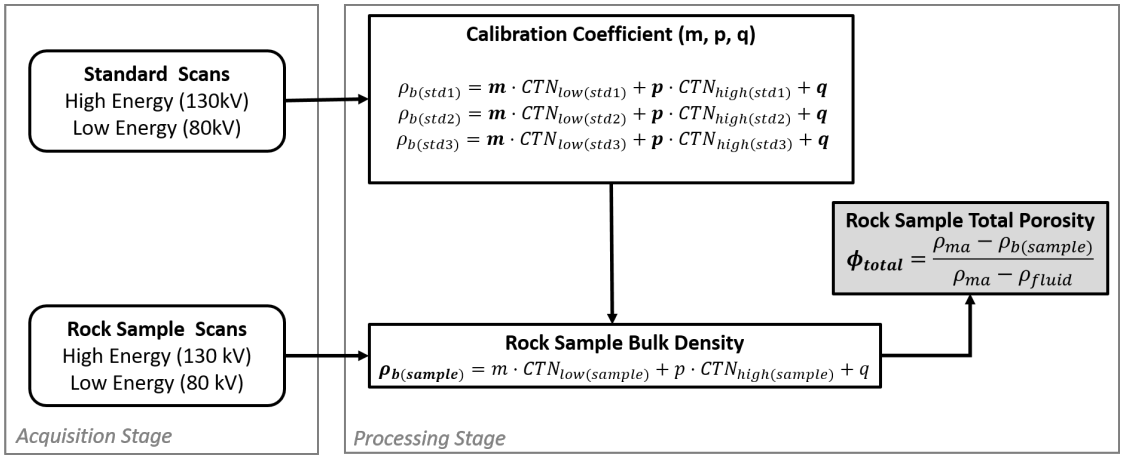

Figure 7: Workflow for DECT bulk density and total porosity determination

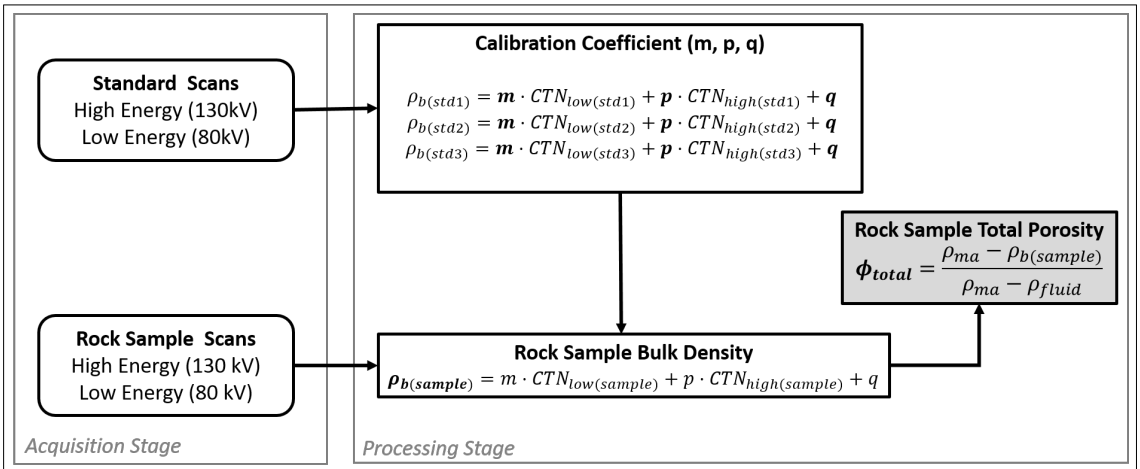

Figure 8: Workflow for DECT effective atomic number determination

rule to determine the calibration coefficients m, p, and q. A similar procedure was applied to derive the calibration coefficients r, s, and t for effective atomic number estimation, as described in Eq.(4). Once these coefficients were established, they enabled the estimation of bulk density and effective atomic number for the rock samples.

$$\rho_b = m \cdot \mathrm{CTN}_{\mathrm{low}} + p \cdot \mathrm{CTN}_{\mathrm{high}} + q \tag{3}$$

$$Z_{\mathrm{eff}} = \left(\frac{r \cdot \mathrm{CTN}_{\mathrm{low}} + s \cdot \mathrm{CTN}_{\mathrm{high}} + t}{0.9342 \cdot \rho_b + 0.1759}\right)^{\frac{1}{3.6}} \tag{4}$$

Finally, to estimate the total porosity (ϕ_{total}) from the determined bulk density by DECT, Eq.(5) is used ($\rho_b = \rho_{\mathrm{fluid}} \cdot \phi_{\mathrm{total}} + \rho_{\mathrm{ma}} \cdot (1 - \phi_{\mathrm{total}})$), this equation include the matrix density matrix (ρ_{ma}), which can estimated from X-ray fluorescence (XRF) data or calculated from basic petrophysical measurements (mass and volume), and the fluid density fluid (ρ_{fluid}), generally considered to be air (0.001 g/cm^3) or nitrogen (0.00125 g/cm^3) for dry samples. Figure 9 presents a sensitivity analysis showing the influence of matrix and fluid densities on dual-energy porosity estimation. Starting with the fluid density, since the densities of air and nitrogen are very close (differing only in the fourth decimal place), their influence on DECT-

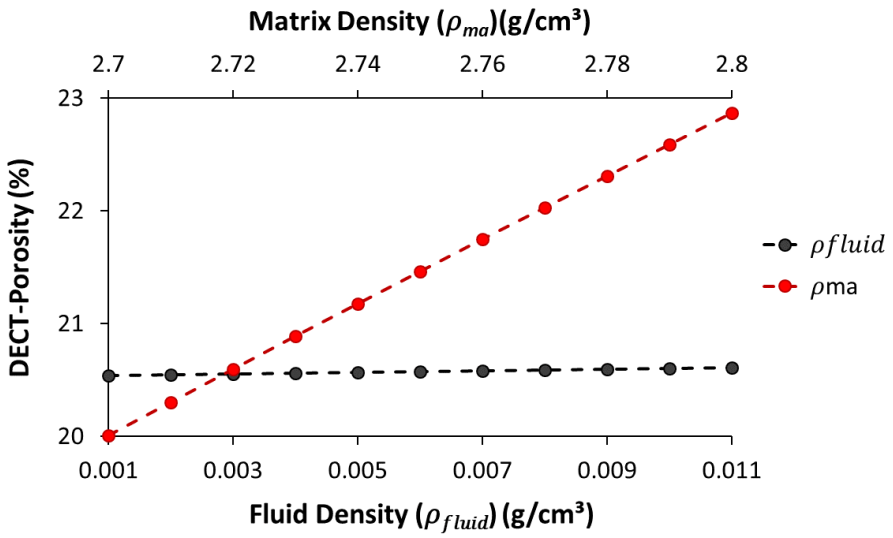

Figure 9: Sample 1. Sensitivity of DECT-porosity to variations in matrix and fluid densities

porosity is negligible. In contrast, the range of matrix (grain) density typically observed in carbonate rocks from 2.7 to 2.8 g/cm^3 [37], has a significant impact on porosity estimation. A variation of just 0.1 g/cm^3 in matrix density results in approximately a 3% change in DECT-porosity.

$$\phi_{\text{total}} = \frac{\rho_{\text{ma}} - \rho_b}{\rho_{\text{ma}} - \rho_{\text{fluid}}} \tag{5}$$

2.5. Single-energy CT technique (SECT)

Figure 10 demonstrates the application of the SECT technique, which enhances the contrast of the connected pore network by subtracting the dry scan (air-filled sample) from the saturated scan (brine-filled sample). Figure 10a and b, show the differences in grayscale values due to fluid content. Into the highlighted red circle, The dry sample image exhibits darker tones in porous regions due to lower attenuation of air, while the saturated sample image, appears lighter in those regions because of the increased X-ray attenuation from the doped brine solution. When the saturated and dry images are subtracted Figure 10c, the connected pore space becomes more distinguishable as lighter areas, effectively highlighting fluid-accessible regions within the rock. This image processing approach enables better detection and quantification of effective porosity, particularly in complex carbonate rocks where the contrast between phases is often limited at medical-CT resolution. This approach is also widely applied in sample images from micro-CT resolution, resulting in a 3D porosity map that closely matches experimental results obtained by a gas porosimeter [3].

An important aspect to consider when using SECT is the selection of the dopant for the saturated brine solution, ensuring it can be effectively distinguished within the rock sample [26, 22, 16]. In this work, we used a brine doped with NaI (30 g/L) [8] for saturating and imaging the samples. Both conditions (saturated and dry) were maintained at the same pressure (14.7 psi) and temperature (20 °C). Using these images and determining the CT number (CTN) of the fluids present under both conditions, it is possible to estimate the effective porosity ϕ_{eff} of the sample by applying Eq.(6) [20, 24].

$$\phi_{\text{eff}} = \frac{\text{CTN}_{\text{saturated}} - \text{CTN}_{\text{dry}}}{\text{CTN}_{\text{doped\_brine}} - \text{CTN}_{\text{air}}} \tag{6}$$

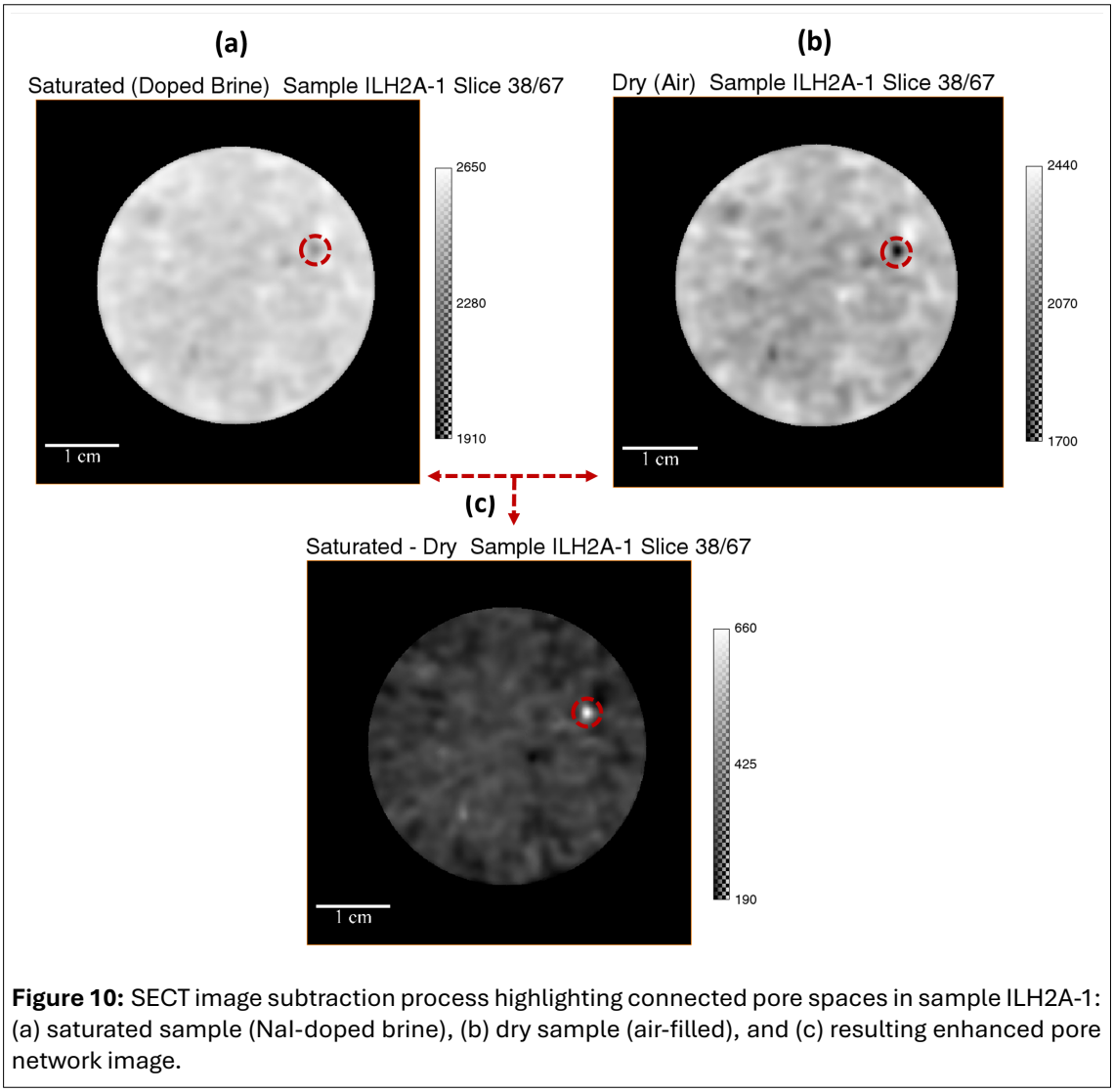

Figure 10: SECT image subtraction process highlighting connected pore spaces in sample ILH2A-1: (a) saturated sample (NaI-doped brine), (b) dry sample (air-filled), and (c) resulting enhanced pore network image.

3. PETROPHYSICAL RESULTS THROUGH DIGITAL IMAGES

The application of digital image analysis using dual-energy (DECT) and single-energy computed tomography (SECT) enabled a comprehensive petrophysical characterization of the Indiana limestone samples. The DECT methodology provided 2D and 3D spatial distributions of key properties, such as bulk density (ρ_b), total porosity (ϕ_{total}), and effective atomic number (Z_{eff}), while SECT focused on determining effective porosity (ϕ_{eff}), associated with connected pore space. Starting with the dual-energy CT (DECT) analysis, Figure 11 shows the standard calibration materials used to determine the DECT coefficients, which are essential for accurately estimating both bulk density and effective atomic number. Aluminum (AL), polytetrafluoroethylene (PTFE), and polyether ether ketone (PEEK) were selected as calibration materials and scanned inside a glass holder equipped with centralizers, using both low- and high-energy protocols described in Table 2. After the scanning and image reconstructing process, the average CTN of each material were calculated. As expected, materials with higher density, such as aluminum, showed significantly greater X-ray absorption, resulting in higher CTN values. By combining the known bulk density and effective atomic number of each standard material with the calculated CTN values (high and low), it is possible to apply Eq.(3) and Eq.(4) to determine the calibration coefficients of the technique. The results are shown in Figure 11.

There is a strong correlation between X-ray attenuation and the density of the material it passes through. Depending on the scanner's detectors and resolution, this attenuation is recorded in sub-volumes (voxels). In the case of DECT, the technique uses both low- and high-energy attenuation values (CT numbers,

Standard Material	ρ_b (g/cm^3)	Z_{eff}
PEEK	1.31	14.14
PTFE	2.15	8.45
AL	2.71	13.00

DECT Calibrations Coeff.	Value
m	-2.85
p	4.37
q	999.72
r	34346.01
s	-33345.06
t	1232369.93

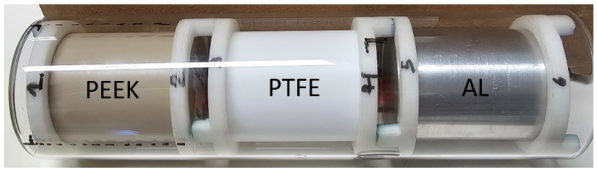

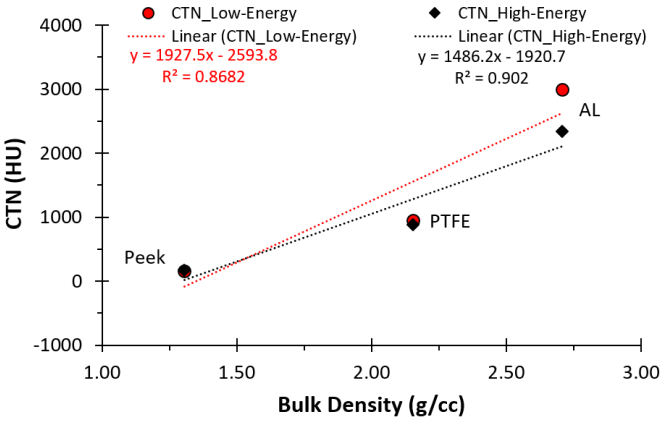

Figure 11: Standard materials used for DECT calibration and determination of the coefficients in Eq.(3) and Eq.(4). The plot demonstrates a strong correlation between CTN and bulk density.

CTN) as input to predict the bulk density of each voxel. It is important to highlight the prior calibration process, which is crucial for the method's accuracy. As shown in Figure 11, the relationship between attenuation values and bulk density is quantified by the coefficients of determination, with R^2 = 0.9020 for high energy and R^2 = 0.8682 for low energy, demonstrating a strong correlation between CT number and bulk density. The difference (ΔR^2) can be attributed to perturbations in the average CTN values at low energy. This effect is evident in the plot for the aluminum standard (Al), which shows a low-energy attenuation (CTN) of 2994 HU compared to 2344 HU at high energy. The difference arises because aluminum, being a denser material (2.71 g/cm^3), partially absorbs the polychromatic low-energy X-ray beam. This behavior increases the attenuation at low energy and is directly related to the beam hardening effect. Since the total porosity equation (Eq.(5)) includes measured values for the solid matrix and pore fluid densities, as well as the estimated bulk density of the sample, a final calibration was performed. This bulk density calibration employed an empirical relationship between the measured and DECT-estimated bulk densities. The calibration relationship was derived using reference materials with well-known properties, as shown in Figure 12.

After the calibration step was carried out (i.e., obtaining the calibration coefficients), all rock samples were scanned using the dual-energy protocol under the same conditions as the calibration materials (within a glass holder at atmospheric pressure and room temperature). The DECT equations (Eq.(3), Eq.(4), and Eq.(5)) were then applied to determine the petrophysical properties of the carbonate samples, from porosity estimations the matrix density was defined as 2.72 g/cm^3, based on mineralogical composition determined from X-ray fluorescence (XRF) analysis reported in the literature [17], and the fluid density was set to 0.001 g/cm^3, corresponding to the density of air. Table 3 summarizes the results obtained from the DECT technique for each sample. Total porosity values ranged from 16.1% to 21.3%, with differences of up to 8.43% compared to gas-porosimeter measurements. It is important to note that the gas porosimeter measures effective porosity, while the DECT technique estimates total porosity (including both connected and isolated pores). Additionally, our DECT-based porosity estimation was performed on a volume of interest (VOI) representing approximately 89% of the total sample volume, following the masking pre-processing step.

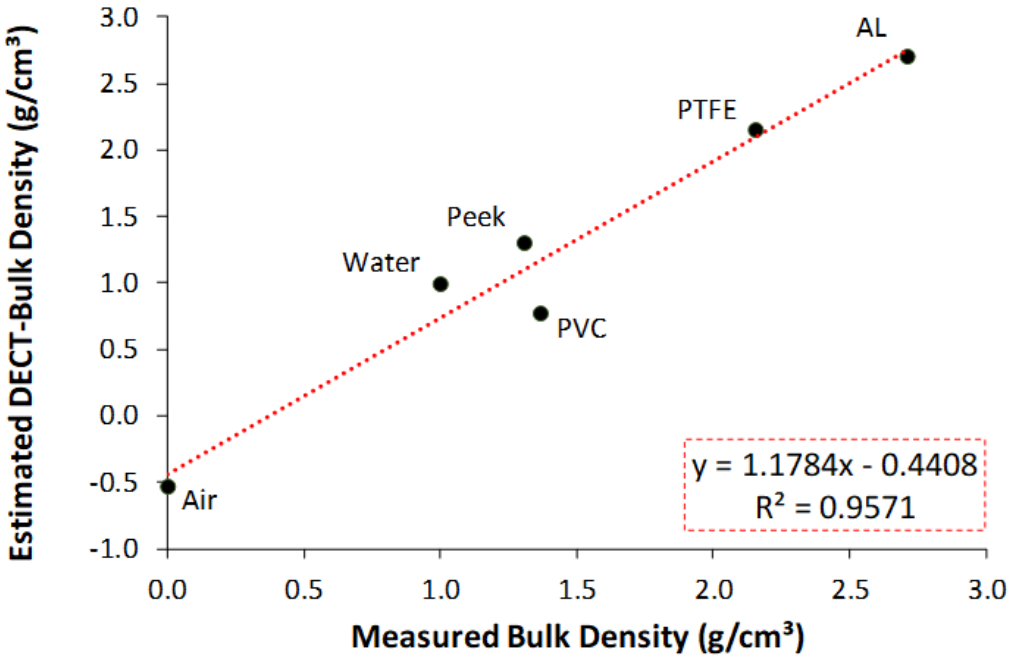

Figure 12: Empirical calibration between DECT-estimated and measured bulk densities using standard reference materials.

Table 3: DECT petrophysical results for rock samples, including percentage differences compared to basic petrophysics measurements.

Sample Number	Total Porosity ϕ_{total} (%)	Difference (%)	Bulk Density ρ_b (g/cm^3)	Difference (%)	Eff. Atomic Number Z_{eff}	Difference (%)
1	20.4	11.5	2.16	0.47	14.5	5.80
2	16.6	5.14	2.27	5.09	14.2	3.31
3	16.1	9.55	2.28	6.05	14.2	3.26
4	16.8	4.55	2.26	5.12	14.3	3.51
5	19.5	8.33	2.19	2.34	14.5	5.19
6	21.3	11.5	2.14	0.94	14.6	6.85
Average	18.5	8.43	2.22	3.34	14.4	4.65

Bulk density and effective atomic number estimates exhibited percentage differences of 3.34% and 4.65%, respectively, when compared with bulk density determined via gravimetric method (mass-to-volume ratio), and with mineralogical results of Indiana limestone lithology obtained through X-ray fluorescence, as reported in the literature [17]. These results indicate the good performance of the DECT technique, demonstrating its ability to produce results closely aligned with conventional laboratory methods, even when applied to larger samples at medical-CT resolution.

Visual representations of DECT results for sample 1 are shown in Figure 13 and Figure 14. In Figure 13, the 2D maps illustrate properties variations across internal selected slices of the core sample. The petrophysical properties maps were generated using the high- and low-energy CT images as inputs, processed through the DECT calibration workflows. Variations in colormap intensity reflect the spatial distribution of these properties, allowing the identification of zones with higher and lower values of total porosity, bulk density, and effective atomic number.

Figure 14 presents the 3D reconstruction of petrophysical properties for sample 1, together with their profiles along the sample length. These visualizations highlight heterogeneities and spatial variations in properties such as bulk density, total porosity, and effective atomic number. The results confirm the

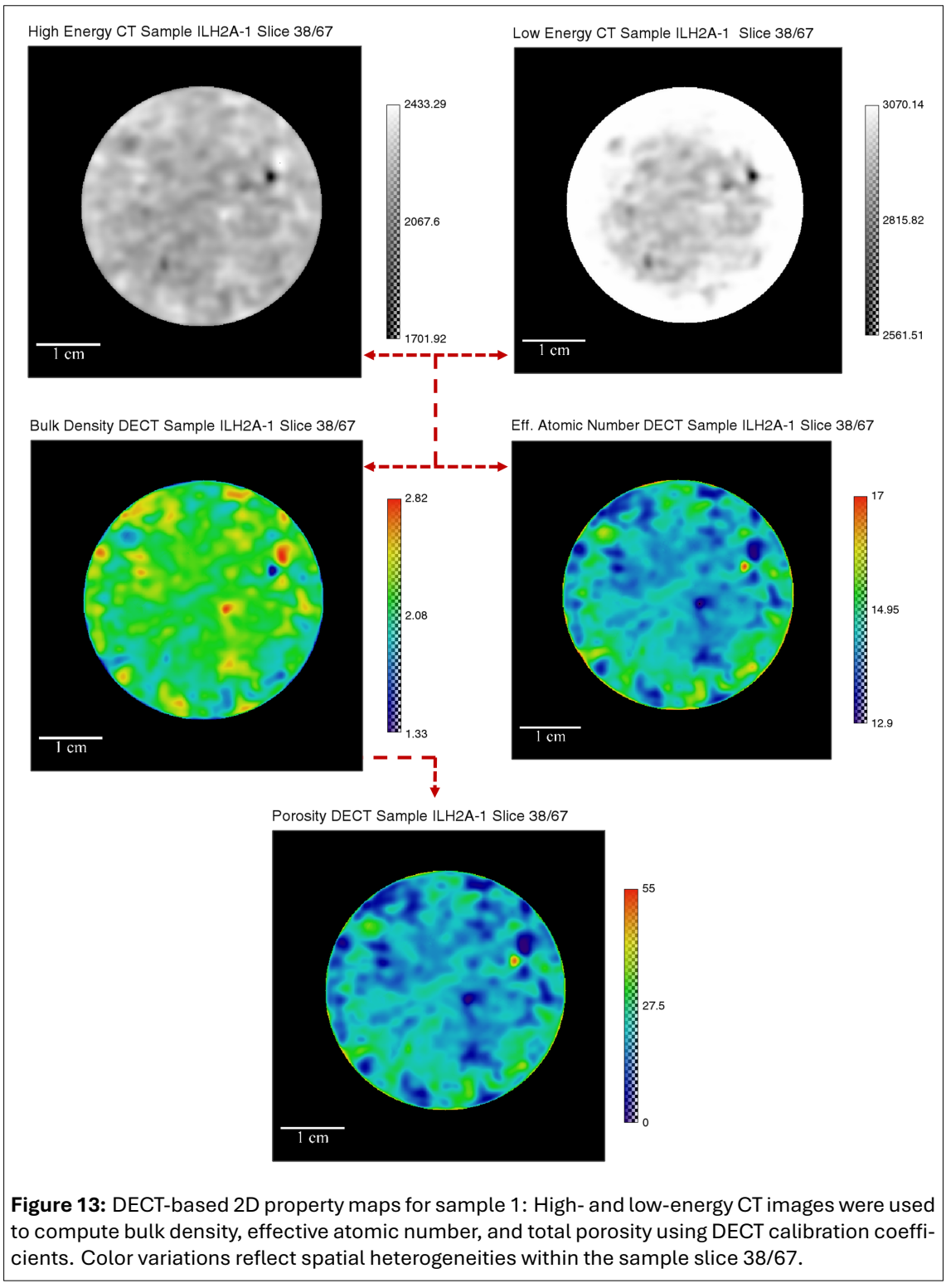

Figure 13: DECT-based 2D property maps for sample 1: High- and low-energy CT images were used to compute bulk density, effective atomic number, and total porosity using DECT calibration coefficients. Color variations reflect spatial heterogeneities within the sample slice 38/67.

capability of the DECT technique to detect spatial trends and local deviations in rock properties, which is particularly valuable for characterizing heterogeneous carbonate formations.

The effective porosity results obtained using the SECT technique for the six analyzed Indiana limestone samples and their average are included in Table 4. Effective porosity (ϕ_{eff}) values ranged from 16.1% to 18.7%, with a percentage differences of 5.30% compared to gas porosimeter measurements. It is important to highlight that these results correspond to a volume of interest (VOI) representing approximately 89% of the total sample volume. The relatively low deviation from basic petrophysics demonstrate the

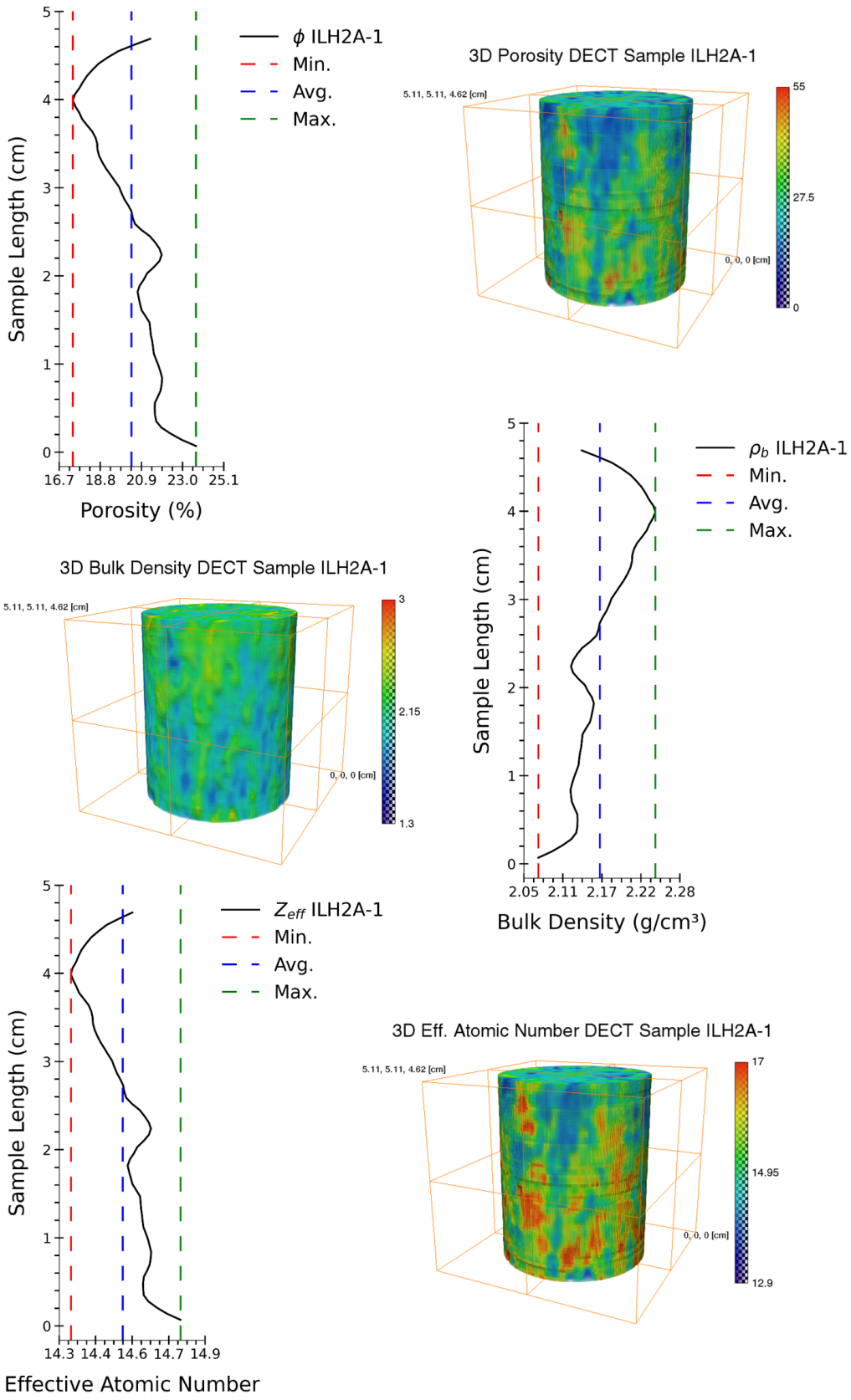

Figure 14: 3D maps and axial profiles of total porosity, bulk density, and effective atomic number for sample 1 obtained via DECT. Vertical profiles show property variations along the core length, with reference lines indicating minimum, average, and maximum values.

Table 4: SECT effective porosity results for Indiana limestone samples, including percentage differences relative to gas porosimeter measurements, along with uncertainties from DECT, SECT, and porosimeter methods.

Sample Number	DECT Total Porosity ϕ_{total} (%)	SECT Effective Porosity ϕ_{eff} (%)	Porosimeter Effective Porosity ϕ_{eff} (%)	Differences (%)
1	20.38 ± 10.02	18.68 ± 4.36	18.27 ± 0.37	2.19
2	16.59 ± 9.97	16.46 ± 4.42	17.48 ± 0.37	5.71
3	16.12 ± 9.69	16.15 ± 4.28	17.73 ± 0.37	9.55
4	16.78 ± 9.15	16.38 ± 4.01	17.60 ± 0.37	6.82
5	19.54 ± 13.08	17.39 ± 5.65	17.97 ± 0.36	3.33
6	21.34 ± 9.86	18.34 ± 4.44	19.13 ± 0.38	4.19
Average	18.45	17.24	18.03	5.30

reliability and accuracy of the SECT method in quantifying effective porosity from medical-CT images, supporting its potential use for larger-scale petrophysical characterization.

In terms of uncertainty, the three methods diverge. DECT involves multiple arithmetic stages: obtaining the calibration coefficients (m, p, q) from standards (Eq.(3), solved by Cramer's rule) with the standards' CT and density uncertainties; predicting bulk density for rock sample using the low- and high-energy CT number (CTN) and calibration coefficients uncertainties; and finally estimating total porosity (Eq.(5)), which also depends on uncertainties of matrix density (from X-ray fluorescence) and fluid density. Each step adds variance, and this propagation of uncertainties explains the larger deviation in DECT total porosity reported in Table 4 (±9 to 13%). SECT, in contrast, applies a single ratio (Eq.(6)), propagating only the standard deviations of the high-energy CTN of the saturated and dry samples and the CTN of brine and air fluid references, as a results its uncertainties are more compact (±4 to 6%). Finally, gas porosimeter is a direct measurement, accounting uncertainties for pore volume as a function of pressure and the dead volume of the equipment; therefore exhibits the smallest deviation (±0.36 to 0.38%).

The SECT and DECT techniques were further compared in Figure 15 through porosity profile analysis of sample 1. This comparison shows consistency between the two approaches in identifying regions of increased pore volume, although SECT focuses on the connected pore system while DECT includes both connected and isolated pores. Together, these results demonstrate that medical-CT imaging, despite the image lower resolution, is capable of delivering estimates of key petrophysical parameters. The combined use of DECT and SECT enhances interpretation by distinguishing between total and effective porosity, a crucial aspect for evaluating fluid flow potential in carbonate reservoirs.

Porosity estimations from SECT and DECT, along with gas porosimeter measurements, for the six Indiana limestone samples are summarized in the radar plot shown in Figure 16. The results highlight samples 1, 5, and 6, where SECT effective porosity (ϕ_{eff}) closely matches gas porosimeter measurements, and the DECT total porosity (ϕ_{total}) results are above the porosimeter measurements. In contrast, samples 2, 3, and 4 present SECT and DECT estimations with greater deviation from gas porosimeter measurements. This discrepancy can be partially attributed to the 11% of the sample volume not analyzed, as the volume of interest (VOI) comprises only 89% of the total sample volume.

Finally, porosity maps obtained through the DECT workflow can help identify unresolved regions within the segmented medical-CT images. As shown in Figure 17, macropores segmented from the medical-CT images of sample 6 (ILH2A-6) accounted for only 0.24% of the total porosity, compared to an average DECT porosity of 21.3%. This indicates that 21.06% of the porosity corresponds to unresolved sub-pixel pores, which cannot be directly visualized at medical-CT resolution. Nevertheless, the DECT porosity maps provide a helpful information to infer the spatial distribution of these sub-resolution pores. By mapping the highest voxel values from the DECT porosity maps (while excluding the already labeled resolved macropores) it is possible to enhance the segmentation by adding an additional label for unresolved regions. These unresolved regions represent zones with potential meso and microporosity, thereby

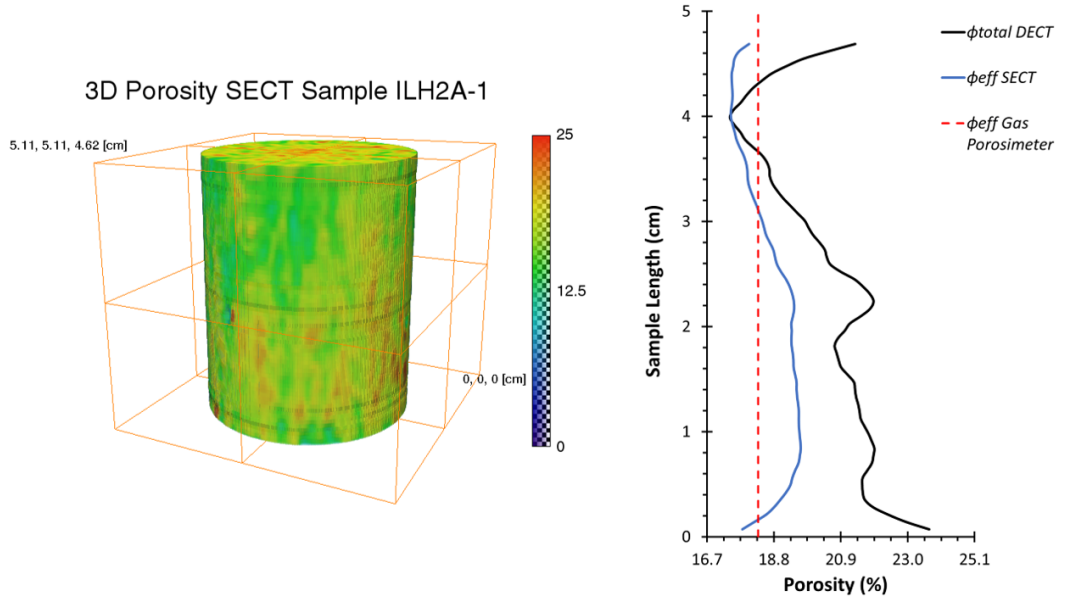

Figure 15: 3D map and axial porosity profiles for sample 1 derived from SECT. The comparison includes total porosity from DECT, effective porosity from SECT, and reference porosity from the gas porosimeter. The profiles highlight spatial variations and the distinction between connected (effective) and total pore volume.

extending the applicability of the segmentation workflow beyond macropore detection and enabling a more realistic pore space characterization, which is important for future permeability estimations. These preliminary results should be validated against higher-resolution images that can directly resolve and quantify meso and micropores within the unresolved regions.

Future work could extend the use of SECT and DECT porosity maps to estimate permeability distributions. One possible approach is to apply analytical models, such as the Kozeny–Carman equation, which relate porosity to permeability by assuming simplified pore geometry (capillary tubes of an effective radius) [15]. The representative pore size needed for this calculation can be obtained from complementary measurements such as MICP or NMR. Another possibility is to integrate porosity maps into multiscale digital rock workflows, where pore-network models capture the connected pores resolved by CT, and unresolved regions are upscaled populating the microporosity detected at higher resolutions (micro-CT and synchrotron-CT) [32, 12]. These approaches, supported by previous studies, provide a way to generate permeability maps and investigate flow behavior from the porosity distributions obtained in this work. Although this was not performed here, we acknowledge it as a limitation and suggest it as future research.

4. DISCUSSION

One of the primary challenges identified in this study relates to the image quality of the low-energy CT scans. As shown in Figure 18, the low-energy image of sample 1 exhibits noticeable artifacts, particularly at the edges of the sample, which can impact the accuracy of CT number extraction and consequently, the computed petrophysical properties. These artifacts mainly arise from beam hardening and reduced X-ray penetration at lower energies. Despite applying filtering techniques and optimizing acquisition parameters, specifically by increasing exposure time and reducing the spiral pitch factor to achieve the maximum effective mAs permitted by our medical-CT scanner, some artifacts remained evident.

Figure 19 provides the quantitative results of statistical analyses for both the inputs (high- and low-energy images) and the outputs (porosity, bulk density, and eff. atomic number maps) obtained from

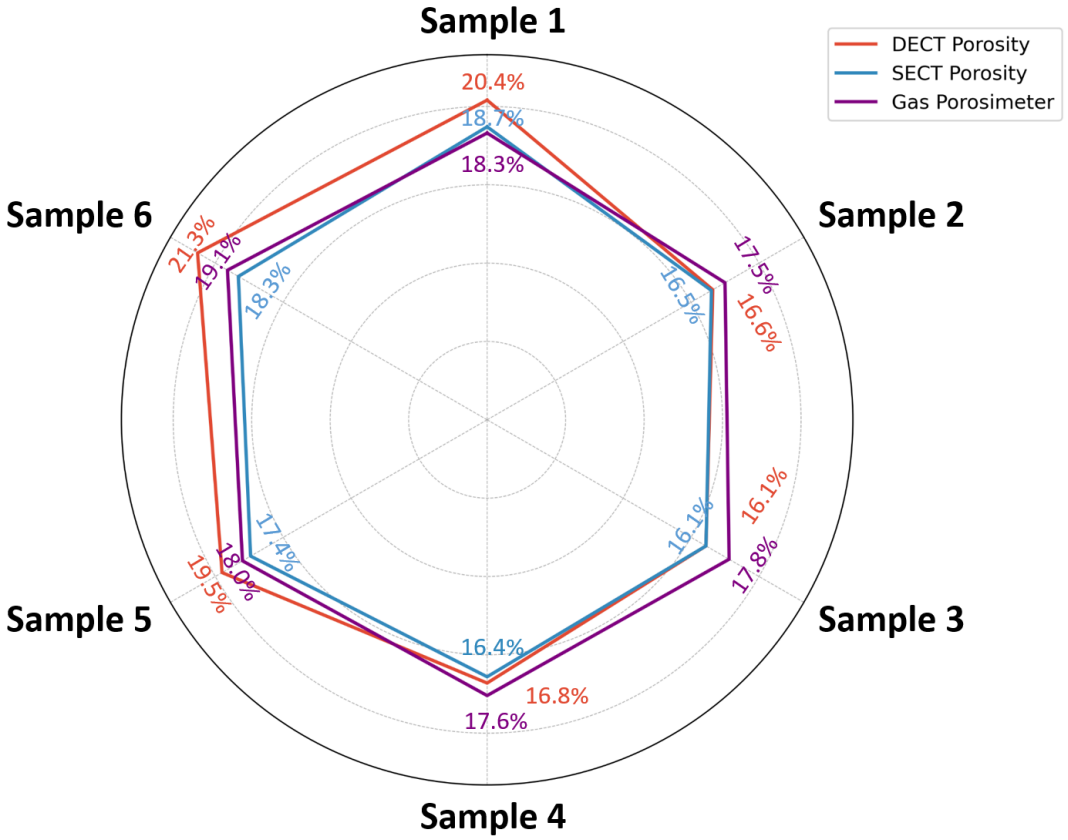

Figure 16: Radar plot comparing porosity estimations from SECT and DECT with gas porosimeter measurements for six Indiana limestone samples.

the dual-energy technique. Following the discussion of how artifacts (beam hardening) affect the CT number of low-energy intensity image, this is evident in its histogram, which displays an anomalous region between 3055 HU and 3075 HU (white region), representing 41% of the total voxels in the image. However, this anomalous region does not appear in the high-energy image, which instead exhibits a well-behaved unimodal histogram. In this context, the derived outputs, such as porosity, bulk density, and effective atomic number, obtained as a function of both low- and high-energy images combined with the calibration process, show acceptable results, as reflected in their respective histograms and standard deviations of 5.84, 0.15, and 0.45.

The beam hardening correction (BHC) module from the commercial software Avizo 3D was tested on the low-energy images of rock sample 1, aiming to correct the artifact-affected region and recover pore information in that zone. However, as shown in Figure 5b, it did not reveal additional pore structure details in the sample image, but only modified the grayscale intensity, shifting the anomalous white tone (3065 HU) to a gray level (2958 HU), as reflected in the histograms of the original and corrected images. This low performance of the module is explained by the heterogeneous nature of the carbonate rock, which contradicts the homogeneity assumption required by the BHC algorithm. Because the method relies on a radial intensity profile normalized by the inner region, mineralogical variations and pore heterogeneity reduce its ability to distinguish beam hardening artifacts, resulting in limited correction efficiency. Therefore, this correction should only be applied to fairly homogeneous samples, as shown in Figure 4a [42].

In addition to the BHC module, another potential approach for mitigating artifacts in CT images is the use of iterative reconstruction (IR) techniques. iterative algorithms incorporate statistical or numerical models of the acquisition process, allowing them to progressively refine the reconstructed image. This

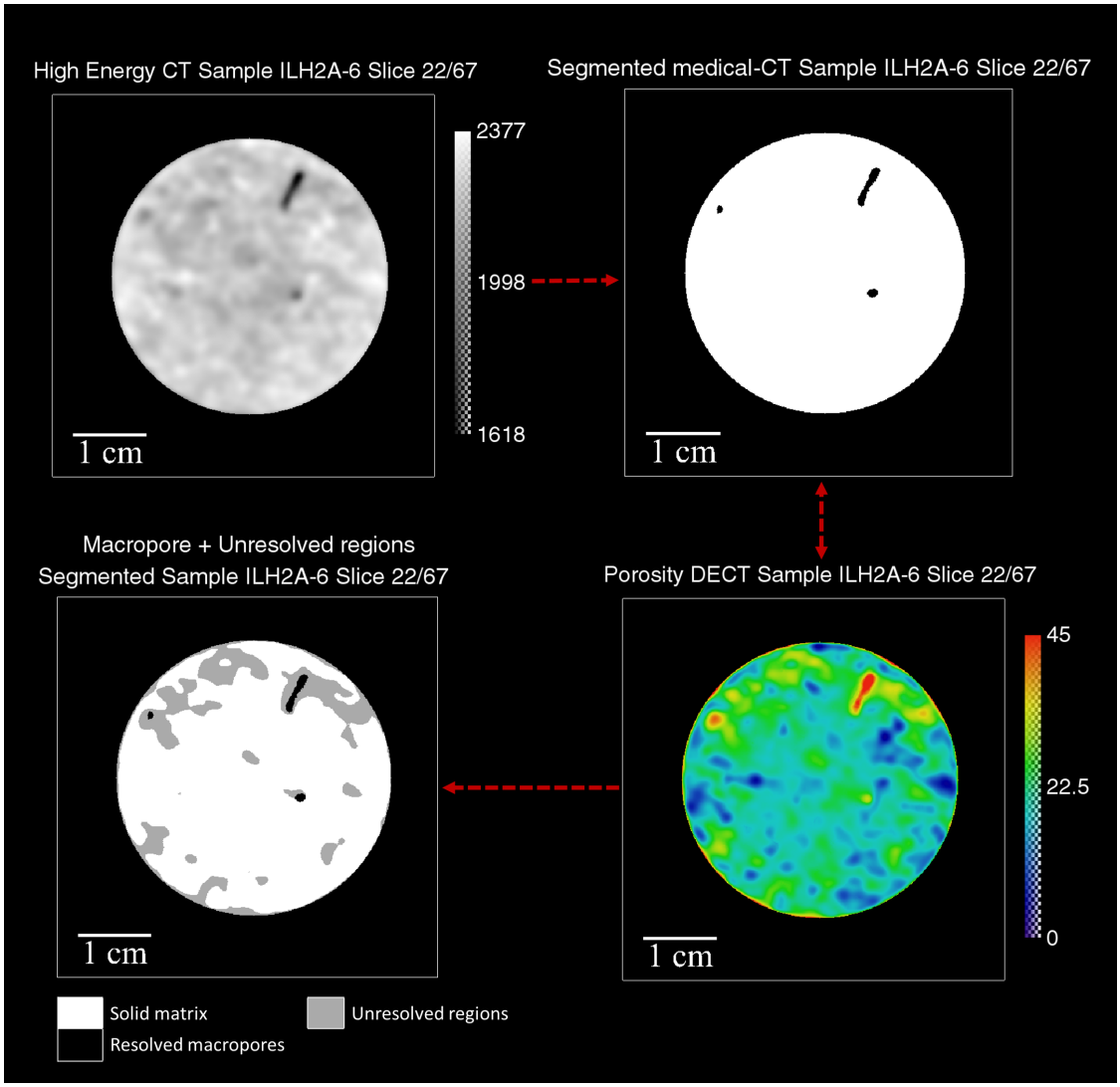

Figure 17: Sample 6. Segmentation workflow supported by DECT porosity maps to identify unresolved regions associated with meso and microporosity not seen at the studied resolution.

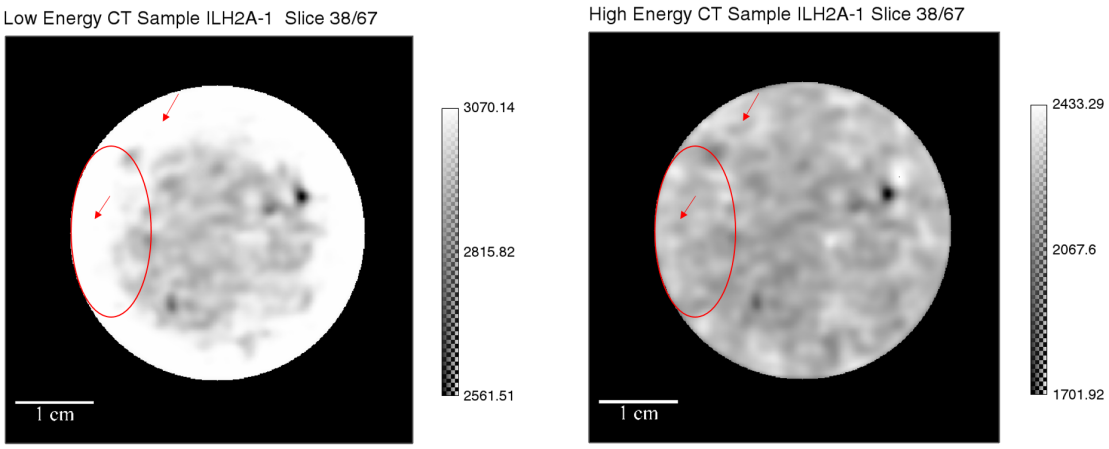

Figure 18: Comparison of image quality between low- and high-energy CT scans of sample 1 (slice 38/67), highlighting the lower image quality in the low-energy scan.

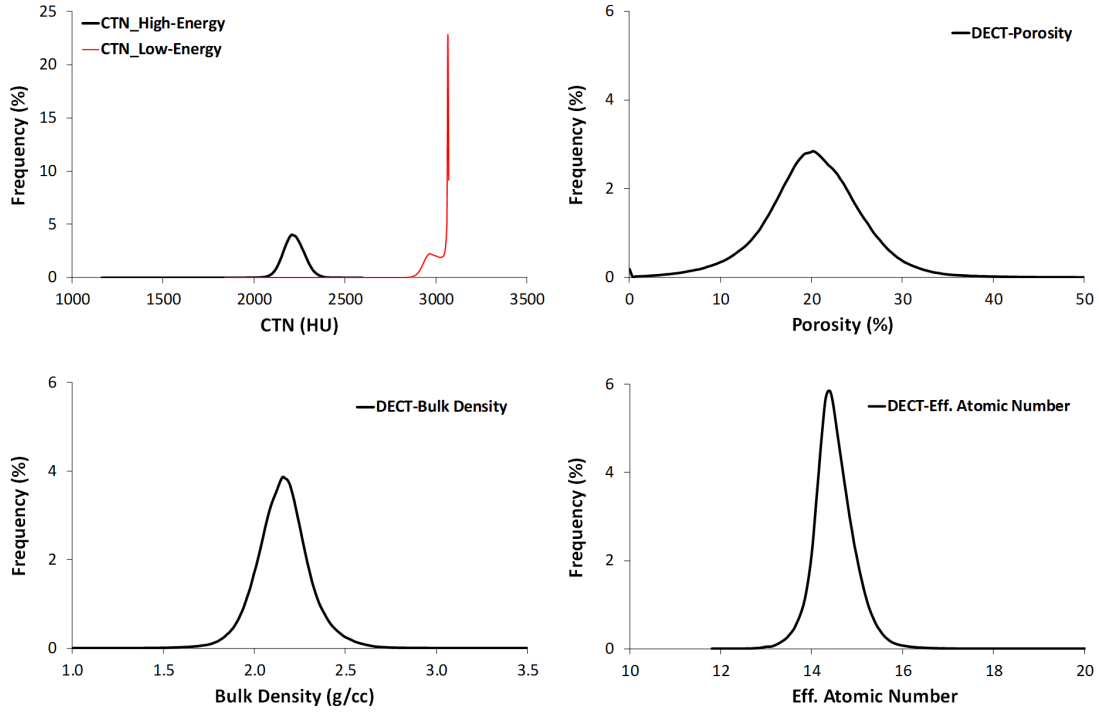

Intensity Image	Average Value	Minimum Voxel Value	Maximum Voxel value	Standard Deviation
CTN_High-Energy (HU)	2223	1166	2606	57.83
CTN_Low-Energy (HU)	3018	1839	3075	53.26
DECT-Porosity (%)	20.39	0.000	84.82	5.840
DECT-Bulk Density (g/cm^3)	2.160	0.410	3.560	0.150
DECT-Eff. Atomic Number	14.53	11.80	25.40	0.450

Figure 19: Sample 1. Statistical analysis of input (low- and high-energy) and output (porosity, bulk density, and effective atomic number) images from the dual-energy technique, highlighting the effect of artifacts in the low-energy histogram.

approach has demonstrated improved performance in reducing artifacts such as beam hardening and ring effects, while enhancing image quality [9, 33]. However, implementing IR methods requires access to the projection data, which were not available in this study. It is important to note that the Siemens SOMATOM® Emotion medical CT scanner used in this work does not provide access to the raw projection data (sinograms), but only to the final reconstructed images obtained through filtered back-projection, as it is designed primarily for clinical applications [13]. Future studies using synchrotron beamlines or industrial scanners, where both raw projection data and reconstruction processes are fully accessible, could apply this approach, allowing more advanced corrections and potentially improving the accuracy of petrophysical property estimation in heterogeneous carbonate rocks.

Another important factor affecting the accuracy of petrophysical property estimation is the selection of the region of interest defined by the masking step in the preprocessing. Figure [**?**] shows how variations in mask diameter influence the calculated values of total porosity, bulk density, and effective atomic number. Results indicate significant variations near the sample edges, where artifacts become more pronounced. Reducing the mask diameter to exclude these problematic regions and concentrating the analysis on the central portion of the sample (highlighted by the purple circle) improved the stability and consistency of property estimations. However, this approach considerably reduces the volume of interest (VOI) from 88.89% to 34.35%, emphasizing the need for careful consideration of mask size selection in image-based petrophysical analyses.

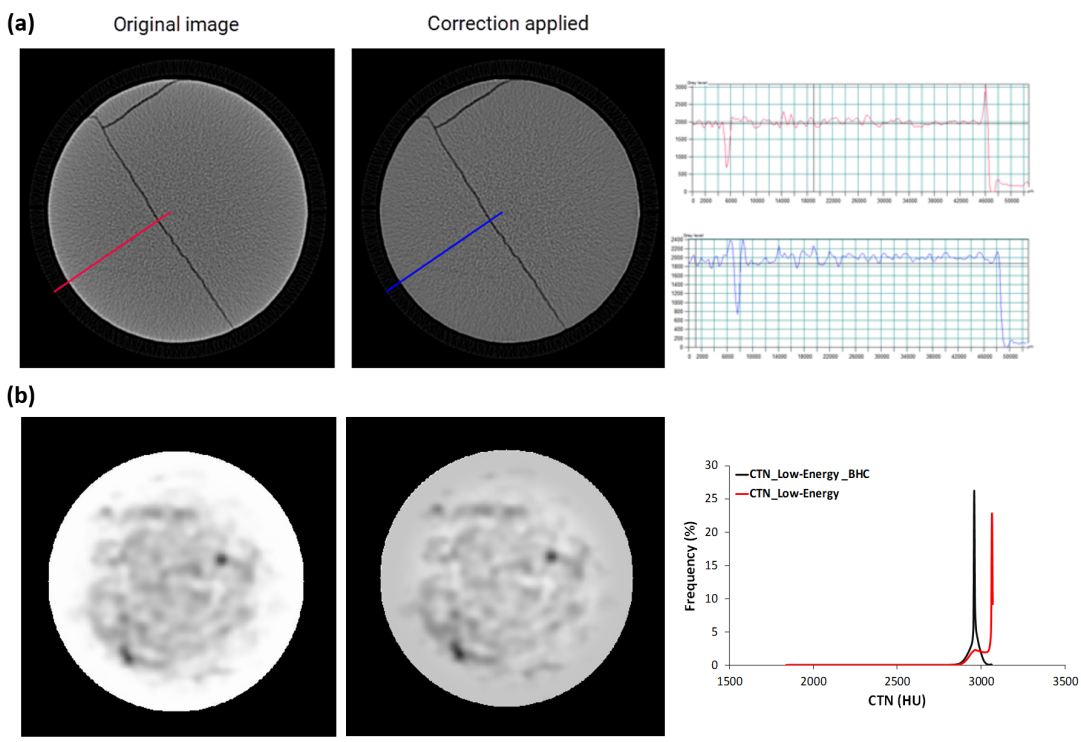

Figure 20: Application of the (a) Avizo 3D beam hardening correction (BHC) module [42] on (b) low-energy images of rock sample 1. The correction shifted grayscale intensity but failed to recover pore details.

In this work, the reduction of the VOI was applied to minimize image artifacts. More generally, VOI reduction (or reducing the sample size) is often performed to achieve higher resolution and enable the detection of micro- and nanopores, particularly when using micro-CT or synchrotron radiation. As shown in Figure 1, achieving micro- and nano-scale resolution that typically requires preparing samples with diameters of around 200 µm [6]. These variations in VOI can be associated with the concept of the deterministic Representative Elementary Volume (REV), which defines the minimum volume required to ensure that the measured properties remain statistically consistent [7]. However, when analyzing carbonate rocks, this reduction can strongly affect representativeness due to their heterogeneous nature. These rocks commonly contain macropores (vugs) up to 200 µm in size [27], which are connected through networks of meso- and micropores. Therefore, selecting and complementing different sample sizes across a wide range of resolutions is essential to capture the full pore size distribution, ensuring statistical reliability of analyses that account for micropores, mesopores, and macropores.

The DECT technique was applied to carbonate rock samples to analyze their complex heterogeneity and spatial distribution of petrophysical properties. However, given the limitations previously reported and discussed, we also tested the methodology on a well-behaved homogeneous sandstone long sample (30 cm in length), specifically a Berea Buff lithology, with its basic petrophysics presented in Figure 22(a). Sample 7 was placed inside an aluminum core holder and pressurized with nitrogen at a pore pressure of 1450 psi, as shown in Figure 22(b). In this setup, the X-ray beam passes through the core holder wall, deionized water, and rubber before reaching the rock sample, with these materials acting as X-ray filters. As the polychromatic beam passes through, the aluminum selectively absorbs lower-energy (softer) photons while allowing higher-energy (harder) photons to pass more easily [25]. These higher-energy photons penetrate the rock sample with less absorption than the low-energy photons, thereby mitigating beam hardening effects in the acquired images.

After the acquisition stage, the low- and high-energy scans were reconstructed, resulting in improved images with mitigated beam hardening artifacts in the low-energy CT, as shown in Figure 23. For com-

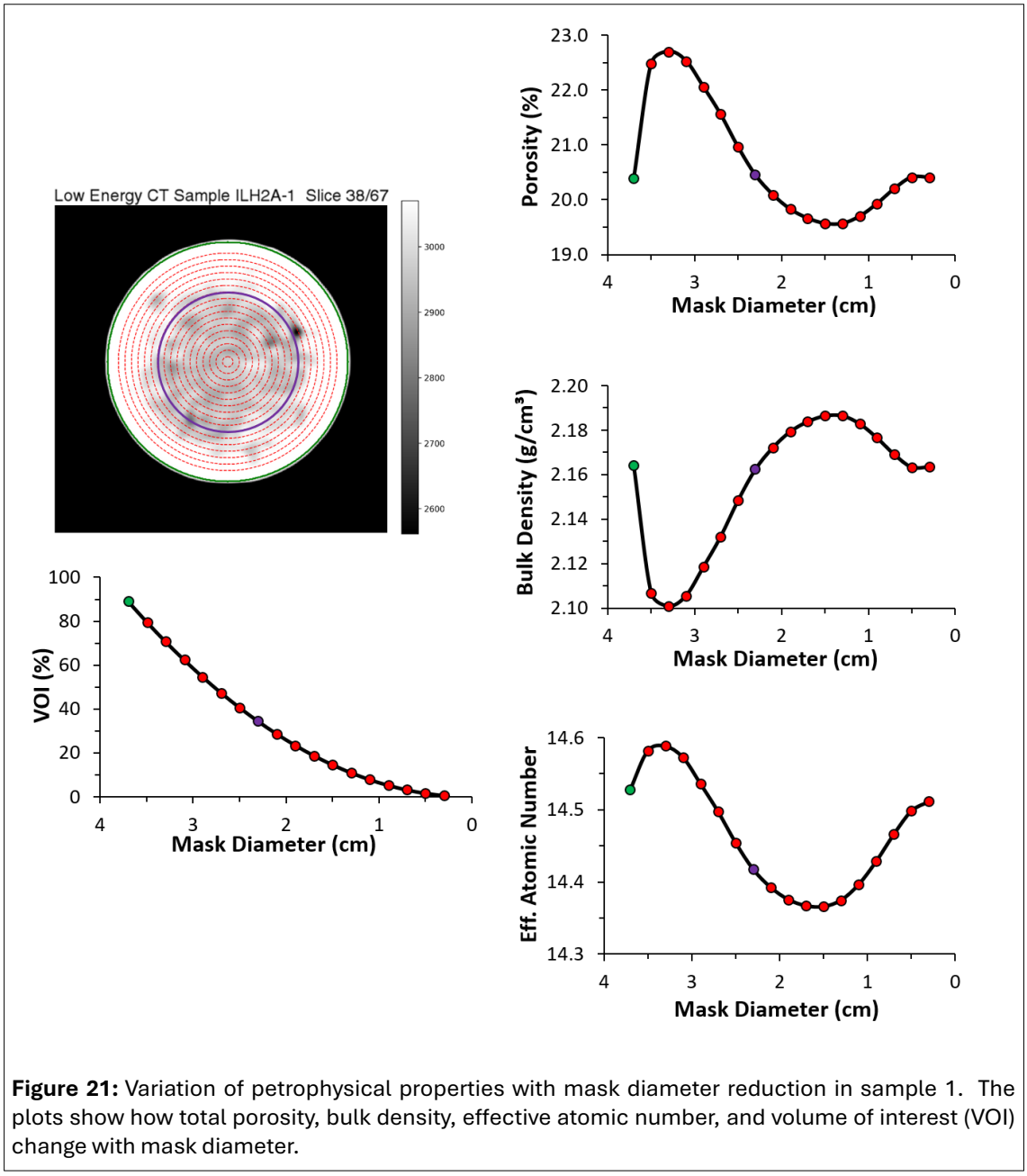

Figure 21: Variation of petrophysical properties with mask diameter reduction in sample 1. The plots show how total porosity, bulk density, effective atomic number, and volume of interest (VOI) change with mask diameter.

parative purposes, its applied the same colormap range (1440 HU to 2426 HU) to the high-energy CT, highlighting the contrast between both images of the same rock sample slice. This difference in attenuation values for the same bulk density, and the calibration process through standards material, ensures the accuracy of the DECT technique. It is also important to note that the calibration standards were re-scanned in this new setup to obtain updated calibration coefficients ($m = -2.10$; $p = 3.44$; $q = 1035.92$; $r = 29424.23$; $s = -27600.87$; $t = 1004228.95$). For porosity estimation (Eq.(5)), a Berea Buff sandstone matrix density of 2.64 g/cm^3 [18], and nitrogen as the pore fluid with a density of 0.00125 g/cm^3 were considered.

The mitigation of beam hardening is confirmed by analyzing the histogram of attenuation values (CTN) in Figure 24, particularly from the low-energy scan, which shows a well-distributed unimodal histogram without perturbations such as secondary peaks. The other property histograms, derived from the DECT methodology for this sandstone sample, estimate accurate average values of 2.12 g/cm^3 for bulk density and 19.73% for porosity, consistent with basic petrophysical measurements. These results reinforce the reliability and applicability of this methodology for the petrophysical characterization of homogeneous

Basic Petrophysics	
Sample Number	7
Sample ID	BE-5A
Diameter (cm)	3.817
Length (cm)	30.05
Bulk Density (g/cm^3)	2.120
Eff. Porosity (%)	19.57
Permeability (mD)	149.8

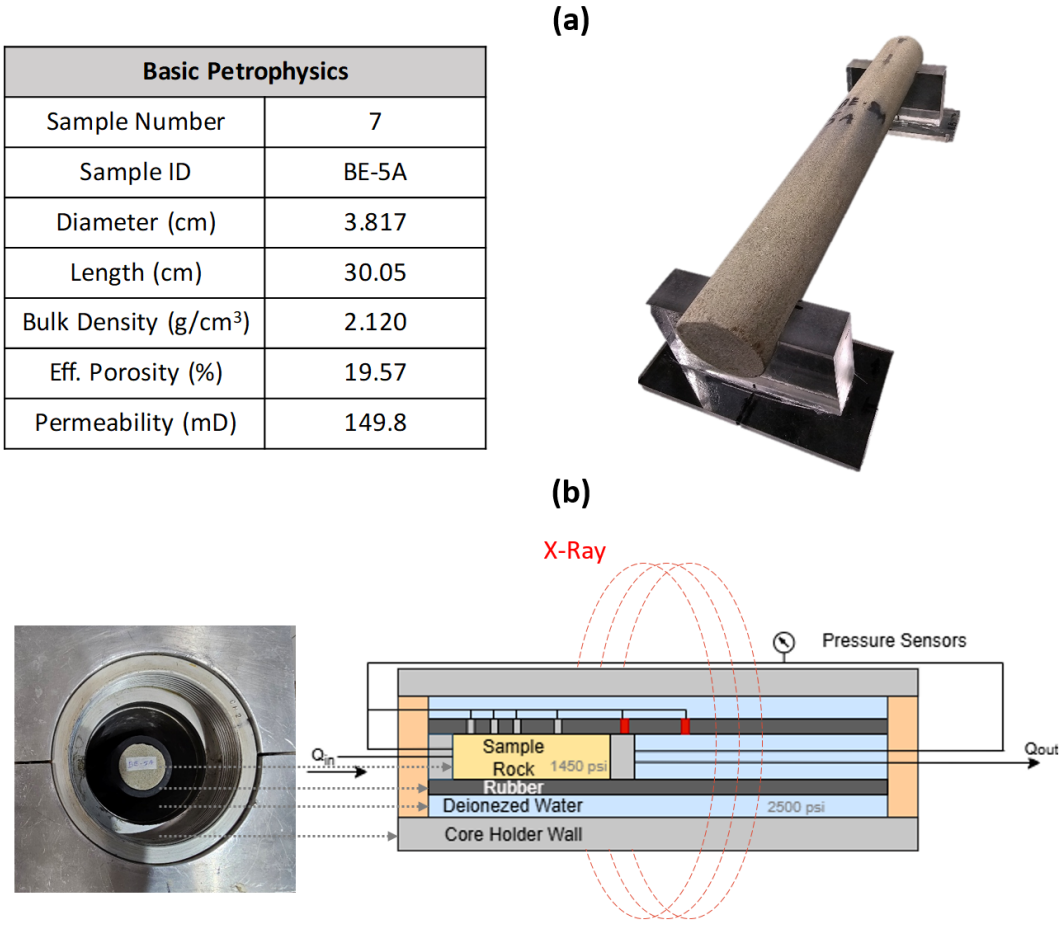

Figure 22: Sample 7. Homogeneous Berea Buff sandstone: (a) basic petrophysics and (b) x-ray acquisition setup.

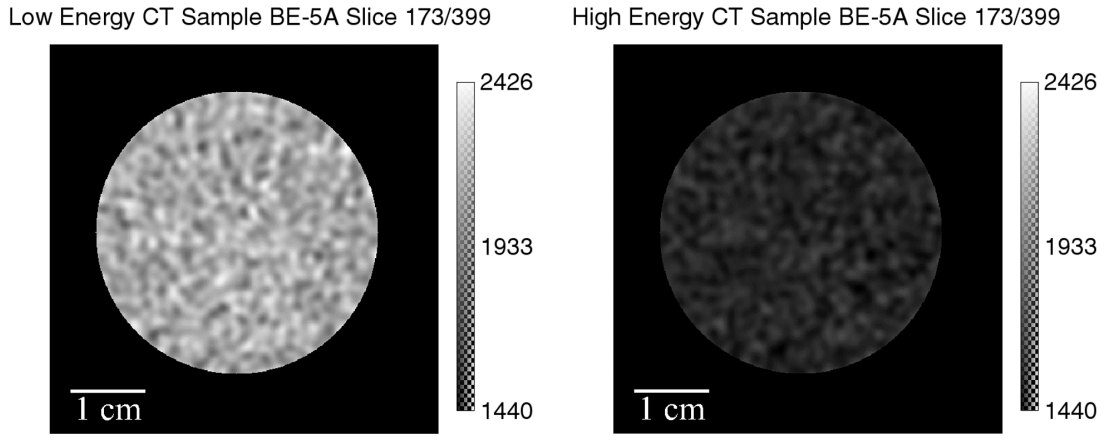

Figure 23: Comparison of image contrast between low- and high-energy CT scans of sample 7 (slice 173/399), highlighting the mitigation of the beam hardening artifact in the low-energy image.

rock samples. Recent work [44], replicated the Dual-Energy CT (DECT) technique on 114 rock samples, including 45 sandstones and 69 carbonates, and demonstrated accurate porosity estimations, further establishing DECT as a robust methodological framework.

Finally, Figure 25 illustrates the 3D and 2D views of the porosity map of sample 7 obtained through the DECT workflow, along with the porosity profile along the sample length. The profile shows values ranging

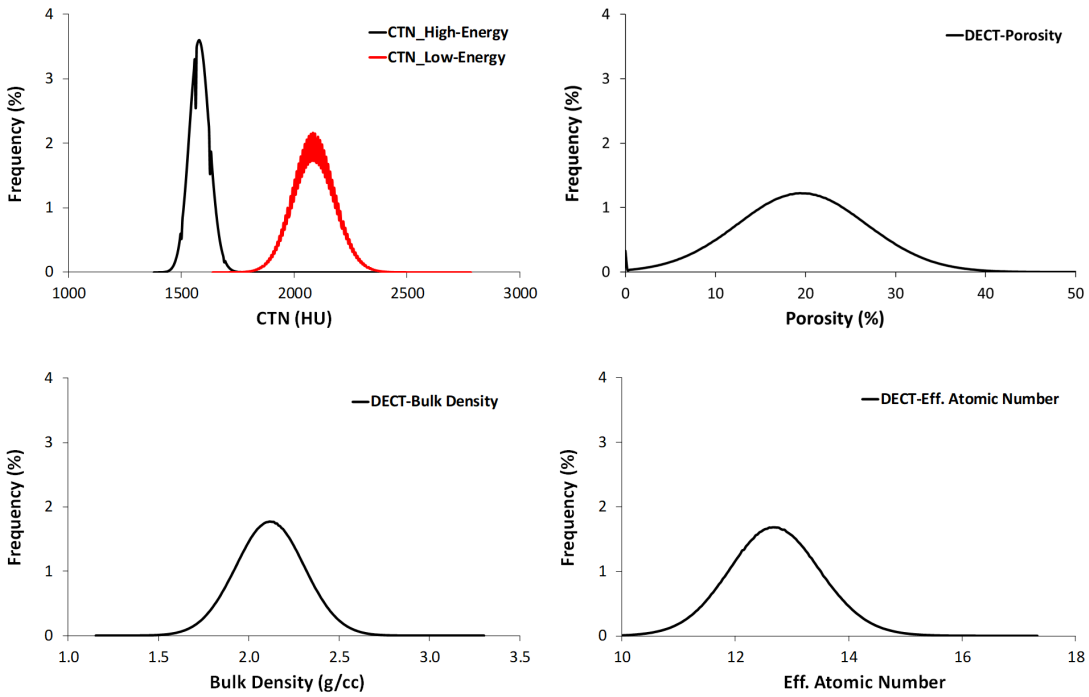

Intensity Image	Average Value	Minimum Voxel Value	Maximum Voxel value	Standard Deviation
CTN_High-Energy (HU)	1583	1379	2387	44.83
CTN_Low-Energy (HU)	2089	1639	2786	92.97
DECT-Porosity (%)	19.73	0.000	56.36	7.180
DECT-Bulk Density (g/cm^3)	2.120	1.150	3.310	0.190
DECT-Eff. Atomic Number	12.72	8.660	17.360	0.820

Figure 24: Sample 7. Statistical analysis of input (low- and high-energy) and output (porosity, bulk density, and effective atomic number) images from the dual-energy technique, highlighting the well distributed histogram of low-energy image.

from 19% to 20%, demonstrating the homogeneous behavior of this sandstone core. The selected 2D slices (6, 173, and 395) display similar spatial porosity distributions, further supporting the homogeneity observed along the core.

This work demonstrates that medical-CT imaging for petrophysical characterization offers a faster and more cost-effective solution, allowing the analysis of considerably larger samples and overcoming cost and time-consuming limitations of high-resolution imaging techniques. The applied methodology provided close estimation of rock sample properties, such as bulk density, effective porosity, and effective atomic number, obtaining percentage differences of 3.34%, 5.30%, and 4.65%, respectively, when compared with bulk density determined via gravimetric method, effective porosity measured using a gas porosimeter, and mineralogical data reported in the literature. Although these findings are promising, they should be considered as preliminary. Further validation, particularly in heterogeneous carbonate rocks, is required to fully establish the reliability and applicability of the method.

The integration of DECT and SECT techniques using medical-CT resolution allowed for the obtention of spatially 2D and 3D maps of petrophysical properties, effectively quantifying and visualizing heterogeneity in Indiana limestone samples. Despite optimizing acquisition parameters and preprocessing steps, the persistence of artifact zones in low-energy CT images and sensitivity of petrophysical estimations to the selection of the volume of interest (VOI) reveal certain limitations of the current methodology. An alternative experimental setup using an aluminum core holder for CT acquisition in a homogeneous sandstone

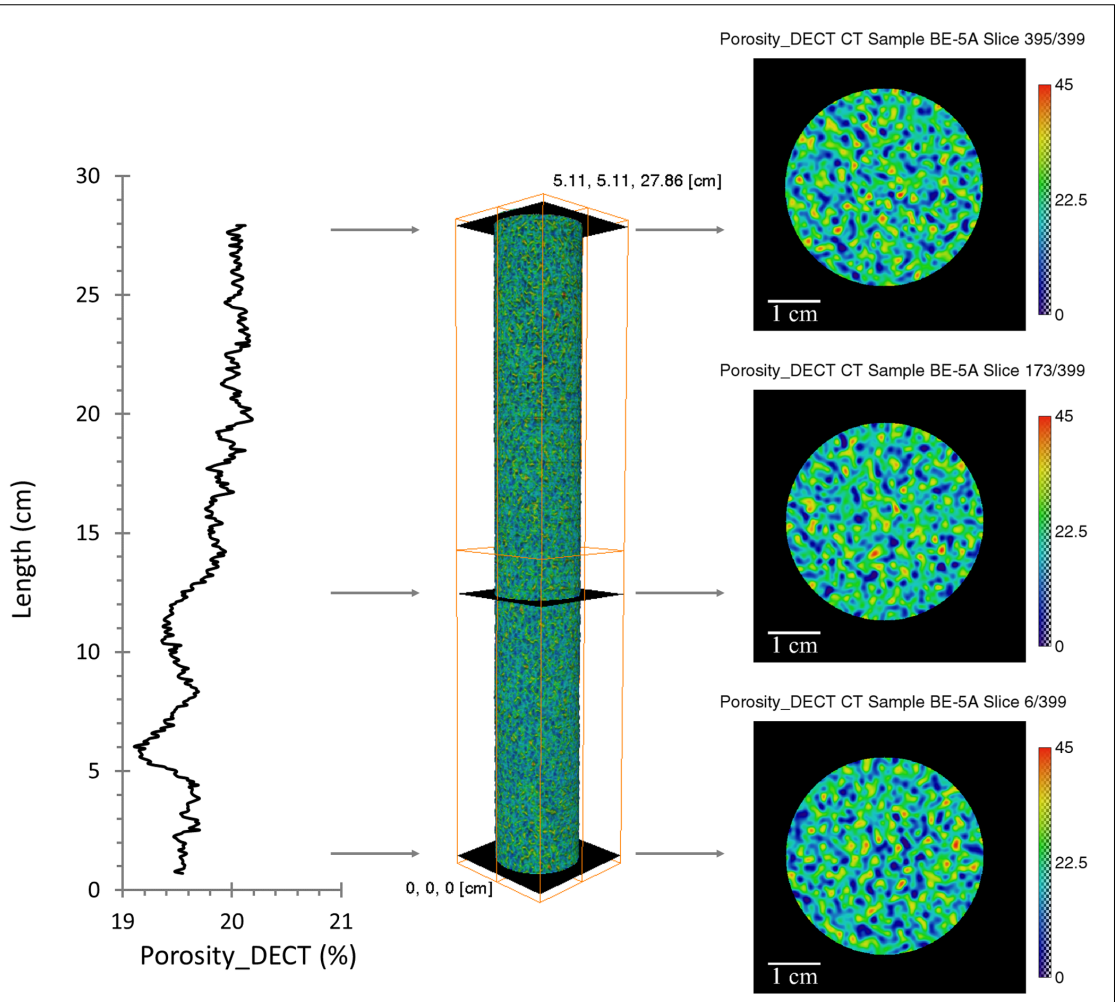

Figure 25: Sample 7. DECT porosity estimation shown in 3D/2D views with corresponding sample profile.

sample demonstrated improved performance of the methodology, minimizing artifacts and providing more accurate petrophysical estimations, enhancing its potential for application in routine petrophysical analyses of homogeneous rock samples.

While this study demonstrates the applicability of medical CT for petrophysical characterization, further validation against high-resolution micro-CT (μ-CT) data is still required to confirm the accuracy of the methodology in heterogeneous carbonate rocks. This effort is already underway in our ongoing research, with preliminary results comparing between medical-CT and μ-CT images were presented in [5]. Future publications will report these and additional findings in greater detail.

STATEMENTS AND DECLARATIONS

Acknowledgments

We gratefully acknowledge the support and sponsorship by Equinor Brazil (Project ANP 23271-0). We also acknowledge the support of ANP (Brazil's National Oil, Natural Gas and Biofuels Agency) through the R&D levy.

Author Contributions

Walter L. F. Antelo: Performed image processing, coding and wrote the manuscript. **Janeth A. Vidal Vargas**: Guided the laboratory test and conducted the CT image acquisition. **Rosangela B. Z. L. Moreno**:

Supervised the research, contributed to the conceptualization of the study, and participated in manuscript revision.

Conflicts of Interest

The authors declare no conflict of interest.

Data, Code & Protocol Availability

All data generated and analyzed during this study, including CT images, properties maps, and python scripts, are available at https://redu.unicamp.br/dataset.xhtml?persistentId=doi:10.25824/redu/ZQOI8E

ORCID IDs

Walter L. F. Antelo: https://orcid.org/0000-0002-4642-9350
Janeth A. Vidal Vargas https://orcid.org/0000-0002-5201-4274
Rosangela B. Z. L. Moreno https://orcid.org/0000-0001-5216-4638

REFERENCES

1. The Role of X-Ray Computed Tomography in Core Analysis, volume All Days of SPE Western Regional Meeting, 05 2003. arXiv:https://onepetro.org/SPEWRM/proceedings-pdf/03WRM/All-03WRM/SPE-83467-MS/2911018/spe-83467-ms.pdf, doi:10.2118/83467-MS.
2. Dual-Energy CT-Scanning Applications in Rock Characterization, volume All Days of SPE Annual Technical Conference and Exhibition, 09 2004. arXiv:https://onepetro.org/SPEATCE/proceedings-pdf/04ATCE/All-04ATCE/SPE-90520-MS/2874708/spe-90520-ms.pdf, doi:10.2118/90520-MS.
3. Synergies Between Laboratory and Digital Rock for Improvement of Digital Rock Models, volume Day 5 Wed, May 22, 2024 of SPWLA Annual Logging Symposium, 05 2024. arXiv:https://onepetro.org/SPWLAALS/proceedings-pdf/SPWLA24/5-SPWLA24/D051S023R009/3409235/spwla-2024-0135.pdf, doi:10.30632/SPWLA-2024-0135.
4. S Akin and A Kovscek. Computed tomography in petroleum engineering research. 2003. URL: http://sp.lyellcollection.org/.
5. W. L. F. Antelo, V. Vargas, and R. B. Z. L. Moreno. Multiscale reconstruction of carbonate rock pore structure using medical and micro-ct imaging [conference poster]. 2025. doi:10.13140/RG.2.2.15904.85761.
6. N. L. Archilha, G. S.R. Costa, G. R.B. Ferreira, G. B.Z.L. Moreno, A. S. Rocha, B. C. Meyer, A. C. Pinto, E. X.S. Miqueles, M. B. Cardoso, and H. Westfahl. Mogno, the nano and microtomography beamline at sirius, the brazilian synchrotron light source. volume 2380. Institute of Physics, 2022. doi:10.1088/1742-6596/2380/1/012123.
7. Y. Bazaikin, B. Gurevich, S. Iglauer, T. Khachkova, D. Kolyukhin, M. Lebedev, V. Lisitsa, and G. Reshetova. Effect of ct image size and resolution on the accuracy of rock property estimates. Journal of Geophysical Research: Solid Earth, 122:3635–3647, 5 2017. doi:10.1002/2016JB013575.
8. Pradeep Bhattad, Benjamin Young, Carl Fredrik Berg, Alf Birger Rustad, and Olivier Lopez. X-ray micro-ct assisted drainage rock typing for characterization of flow behaviour of laminated sandstone reservoirs. In Proceedings of the International Symposium of the Society of Core Analysts (SCA), Avignon, France, September 2014. URL: http://refhub.elsevier.com/S0309-1708(16)30309-8/sbref0005.
9. Loes Brabant, Manuel Dierick, Elin Pauwels, Yoni De Witte, and Luc Van Hoorebeke. Modifications of iterative reconstruction algorithms for the reduction of artefacts in high resolution x-ray computed tomography. pages 111–114, 7 2013.
10. A. Buades, B. Coll, and J.-M. Morel. A non-local algorithm for image denoising. In 2005 IEEE Computer Society Conference on Computer Vision and Pattern Recognition (CVPR'05), volume 2, pages 60–65 vol. 2, 2005. doi:10.1109/CVPR.2005.38.
11. Tom Bultreys, Wesley De Boever, and Veerle Cnudde. Imaging and image-based fluid transport modeling at the pore scale in geological materials: A practical introduction to the current state-of-the-art, 4 2016. doi:10.1016/j.earscirev.2016.02.001.

12. Josue Mauricio Plata Chaves and Rosangela Barros Zanoni Lopes Moreno. Low- and high-resolution x-ray tomography helping on petrophysics and flow-behavior modeling. SPE Journal, 26:206–219, 2 2021. doi:10.2118/202495-PA.
13. Baiyu Chen, Xinhui Duan, Zhicong Yu, Shuai Leng, Lifeng Yu, and Cynthia McCollough. Technical note: Development and validation of an open data format for ct projection data. Medical Physics, 42:6964–6972, 12 2015. doi:10.1118/1.4935406.
14. Anton du Plessis, Stephan Gerhard le Roux, and Anina Guelpa. Comparison of medical and industrial x-ray computed tomography for non-destructive testing. Case Studies in Nondestructive Testing and Evaluation, 6:17–25, 11 2016. doi:10.1016/j.csndt.2016.07.001.
15. Selçuk Erol, Sarah Jane Fowler, Virginie Harcouët-Menou, and Ben Laenen. An analytical model of porosity–permeability for porous and fractured media. Transport in Porous Media, 120:327–358, 11 2017. doi:10.1007/s11242-017-0923-z.
16. Emily Fitzhenry, Richard Martel, Thomas Robert, and Mathieu Des Roches. Dual-energy ct scan protocol optimization to monitor transient fluid saturation distributions during three-phase flow in sand columns. Colloids and Surfaces A: Physicochemical and Engineering Aspects, 645, 7 2022. doi:10.1016/j.colsurfa.2022.128955.
17. Marina Freire-Gormaly, Jonathan S. Ellis, Heather L. MacLean, and Aimy Bazylak. Pore structure characterization of indiana limestone and pink dolomite from pore network reconstructions. Oil and Gas Science and Technology, 71, 2015. doi:10.2516/ogst/2015004.
18. Hany Gamal, Badr S. Bageri, Salaheldin Elkatatny, and Shirish Patil. Investigating the alteration of sandstone pore system and rock features by role of weighting materials. ACS Omega, 6:4100–4110, 2 2021. doi:10.1021/acsomega.0c06256.
19. Patricia Garnier, Rafael Angulo-Jaramillo, David A Dicarlo, Tim W J Bauters, Christophe J G Darnault, Tammo S Steenhuis, J.-Yves Parlange, and Philippe Baveye. Dual-energy synchrotron x ray measurements of rapid soil density and water content changes in swelling soils during infiltration, 1998.
20. Carlos Roberto Holleben. Determinação de porosidade e saturação de fluidos através da tomografia computadorizada de raios-x. pages 1–198, 1993. URL: https://hdl.handle.net/20.500.12733/1581369, doi:10.47749/T/UNICAMP.1993.75955.
21. S. V. Korneev, X. Yang, J. M. Zachara, T. D. Scheibe, and I. Battiato. Downscaling-based segmentation for unresolved images of highly heterogeneous granular porous samples. Water Resources Research, 54:2871–2890, 4 2018. doi:10.1002/2018WR022886.
22. Qingyang Lin, Yousef Al-Khulaifi, Martin J. Blunt, and Branko Bijeljic. Quantification of sub-resolution porosity in carbonate rocks by applying high-salinity contrast brine using x-ray microtomography differential imaging. Advances in Water Resources, 96:306–322, 10 2016. doi:10.1016/j.advwatres.2016.08.002.
23. Claudio Madonna, Beatriz Quintal, Marcel Frehner, Bjarne S.G. Almqvist, Nicola Tisato, Mattia Pistone, Federica Marone, and Erik H. Saenger. Synchrotron-based x-ray tomographic microscopy for rock physics investigations. Geophysics, 78, 2013. doi:10.1190/GEO2012-0113.1.
24. Alejandro Mendieta-Penagos, Luis Reinaldo Rincón-Bautista, and Edwar Herrera-Otero. Quantitative determination of heterogeneity in samples of rock type plug using x-ray computerized tomography. Boletin de Geologia, 41:133–149, 2019. doi:10.18273/revbol.v41n1-2019007.
25. Bruker microCT. X-ray filters in microct imaging method note mn 148, 2022. URL: https://www.foa.unesp.br/Home/pesquisa/escritoriodeapoioapesquisa/mn148_x-ray-filters-in-microct-imaging.pdf.
26. Anderson C. Moreira, Verônica A. Santos, Iara F. Mantovani, José A.B. Cunha Neto, and Celso P. Fernandes. Evaluation of the induced oil remobilization through high and low salinity waterflooding in a porous system via x-ray microtomography. Chemical Engineering Transactions, 86:1159–1164, 2021. doi:10.3303/CET2186194.
27. Abolfazl Moslemipour and Saeid Sadeghnejad. Dual-scale pore network reconstruction of vugular carbonates using multi-scale imaging techniques. Advances in Water Resources, 147, 1 2021. doi:10.1016/j.advwatres.2020.103795.
28. Ronny Pini and Claudio Madonna. Moving across scales: a quantitative assessment of x-ray ct to measure the porosity of rocks. Journal of Porous Materials, 23:325–338, 4 2016. doi:10.1007/s10934-015-0085-8.
29. Anton Du Plessis and Pierre Rossouw. X-ray computed tomography of a titanium aerospace investment casting. Case Studies in Nondestructive Testing and Evaluation, 3:21–26, 2015. doi:10.1016/j.csndt.2015.03.001.
30. Thomas Ramstad, Nasiru Idowu, Cyril Nardi, and Pål Eric Øren. Relative permeability calculations from two-phase flow simulations directly on digital images of porous rocks. Transport in Porous Media, 94:487–504, 9 2012. doi:10.1007/s11242-011-9877-8.
31. Thomas Ramstad, Pål Eric Øren, and Stig Bakke. Simulation of two phase flow in reservoir rocks using a lattice boltzmann method. volume 4, pages 2561–2576, 2009. doi:10.2118/124617-ms.

32. L. C. Ruspini, P. E. Øren, S. Berg, S. Masalmeh, T. Bultreys, C. Taberner, T. Sorop, F. Marcelis, M. Appel, J. Freeman, and O. B. Wilson. Multiscale digital rock analysis for complex rocks. Transport in Porous Media, 139:301–325, 9 2021. doi:10.1007/s11242-021-01667-2.
33. Hongli Shi, Zhi Yang, and Shuqian Luo. Reduce beam hardening artifacts of polychromatic x-ray computed tomography by an iterative approximation approach. Journal of X-Ray Science and Technology, 25:417–428, 2017. doi:10.3233/XST-16187.
34. Shameem Siddiqui. Some useful guidelines for whole core ct-scanning for petrophysical applications. volume 367. EDP Sciences, 1 2023. doi:10.1051/e3sconf/202336701013.
35. Shameem Siddiqui, Hisham A. Nasr-El-Din, and Aon A. Khamees. Wormhole initiation and propagation of emulsified acid in carbonate cores using computerized tomography. Journal of Petroleum Science and Engineering, 54:93–111, 12 2006. doi:10.1016/j.petrol.2006.08.005.
36. B. Singh, A. K. Agrawal, Y. S. Kashyap, and S. C. Gadkari. X-ray synchrotron dual energy imaging for material specific study. volume 1832. American Institute of Physics Inc., 5 2017. doi:10.1063/1.4980415.
37. José Agnelo Soares, Antônio Jorge, Vasconcellos Garcia, Francisco Hilário, Rego Bezerra, José Antônio Barbosa, Anelise Friedrich, Caroline Léssio Cazarin, Louis Dostoievsky Gomes Tabosa, Rayssa Lima, and Costa Coura. Petrophysics and rockphysics of carbonates from brazil and portugal, 2015. URL: www.phoenix.org.br.
38. Luís Sousa, Johanna Menningen, Rubén López-Doncel, and Siegfried Siegesmund. Petrophysical properties of limestones: influence on behaviour under different environmental conditions and applications. Environmental Earth Sciences, 80, 12 2021. doi:10.1007/s12665-021-10064-3.
39. Catherine Spurin, Sharon Ellman, Dane Sherburn, Tom Bultreys, and Hamdi A. Tchelepi. Python workflow for segmenting multiphase flow in porous rocks. Transport in Porous Media, 2024. non-local means filter/The best filtering for this data set was chosen as uniform spatial weighting, the noisestandard deviation set to 3 times the automatically estimated value, a patch size of 3 vox-els, and a search area of 6 voxels. doi:10.1007/s11242-024-02136-2.
40. Hind Sulieman, Mohamed Soufiane Jouini, Mohammad Alsuwaidi, Emad W. Al-Shalabi, and Osama A. Al Jallad. Multiscale investigation of pore structure heterogeneity in carbonate rocks using digital imaging and scal measurements: A case study from upper jurassic limestones, abu dhabi, uae. PLoS ONE, 19, 2 2024. doi:10.1371/journal.pone.0295192.
41. A. P. Teles, I. Lima, and R. T. Lopes. Rock porosity quantification by dual-energy x-ray computed microtomography. Micron, 83:72–78, 4 2016. doi:10.1016/j.micron.2016.02.004.
42. Thermo Fisher Scientific. Amira-Avizo Software 2024.1 User Guide. Thermo Fisher Scientific Inc., 2024. URL: https://www.thermofisher.com/amira-avizo.
43. Rance Tino, Adam Yeo, Milan Brandt, Martin Leary, and Tomas Kron. The interlace deposition method of bone equivalent material extrusion 3d printing for imaging in radiotherapy. Materials and Design, 199, 2 2021. doi:10.1016/j.matdes.2020.109439.
44. V. Vargas, W. L. F. Antelo, and R. B. Z. L. Moreno. Characterization of sandstone and carbonate rocks using dual-energy x-ray computed tomography for sample selection in coreflooding tests. 2025. doi:10.5281/zenodo.16815648.
45. Harold J. Vinegar and Scott L. Wellington. Tomographic imaging of three-phase flow experiments. Review of Scientific Instruments, 58:96–107, 1987. doi:10.1063/1.1139522.
46. Scott L. Wellington and Harold J. Vinegar. X-ray computerized tomography. 1987. doi:10.2118/16983-PA.
47. Ole Petter Wennberg and Lars Rennan. A brief introduction to the use of X-ray computed tomography (CT) for analysis of natural deformation structures in reservoir rocks, volume 459, pages 101–120. Geological Society of London, 2018. doi:10.1144/SP459.10.